

A Multistage Processing Algorithm for Disturbance Removal and Target Detection in Passive Bistatic Radar

F. COLONE, Member, IEEE

University of Rome "La Sapienza"

D. W. O'HAGAN

University College London

P. LOMBARDO, Member, IEEE

University of Rome "La Sapienza"

C. J. BAKER

University College London

The paper examines the problem of cancellation of direct signal, multipath and clutter echoes in passive bistatic radar (PBR). This problem is exacerbated as the transmitted waveform is not under control of the radar designer and the sidelobes of the ambiguity function can mask targets including those displaced in either (or both) range and Doppler from the disturbance. A novel multistage approach is developed for disturbance cancellation and target detection based on projections of the received signal in a subspace orthogonal to both the disturbance and previously detected targets. The resulting algorithm is shown to be effective against typical simulated scenarios with a limited number of stages, and a version with computational savings is also introduced. Finally its effectiveness is demonstrated with the application to real data acquired with an experimental VHF PBR system.

Manuscript received August 8, 2007; revised February 21, 2008; released for publication March 12, 2008.

IEEE Log No. T-AES/45/2/933015.

Refereeing of this contribution was handled by P. Willett.

Authors' addresses: F. Colone and P. Lombardo, Dept. INFOCOM, University of Rome "La Sapienza," via Eudossiana, 18-00184 Rome, Italy, E-mail: (fabiola.colone@infocom.uniroma1.it); D. W. O'Hagan and C. J. Baker, University College London, Torrington Place, London WC1E 7JE, UK.

0018-9251/09/\$25.00 © 2009 IEEE

I. INTRODUCTION

In recent years the use of passive bistatic radar (PBR) for surveillance purposes has received renewed interest, e.g. [1]. PBR exploits an existing transmitter as an illuminator of opportunity. Among all the emitters available in the environment, broadcast transmitters represent some of the most attractive choices for surveillance purposes, owing to their excellent coverage [2–4]. Specifically the most common signals for PBRs in use today are noncooperative FM commercial radio stations since they offer a good trade off between performance and overall system development costs [4–5]. In particular the high transmit powers available from FM broadcast transmitters allows detection ranges of approximately 250 km [4].

For a PBR the transmitted signal is not available directly to the receiver as in conventional monostatic systems and therefore a dedicated and separate receiver channel is required to collect the directly transmitted signal. This is subsequently used as the reference signal and is correlated with the surveillance channel signal for target echo detection. The transmitted waveform is typically a continuous waveform and may exhibit low reflected power levels requiring long integration times to obtain an acceptable signal-to-noise ratio (SNR) [5].

PBR systems exploit existing illuminators of opportunity which results in covert operation, low vulnerability to deliberate interference, reduced pollution of the electromagnetic environment, etc. However, PBR operation does inherently imply that the transmitted waveform is not within the control of the radar designer. This contrasts with the usual case of conventional radar systems, where the transmitted waveform is carefully designed to provide an ambiguity function with appropriate properties (e.g. narrow peak in both range and Doppler and low sidelobes). Due to the variable and unpredictable characteristics of the transmitted FM waveform the sidelobes of the ambiguity function for PBR usually have a time-varying structure and exist at a level not greatly lower than that of the peak [6, 8]. This can lead to: 1) strong clutter echoes masking targets with high Doppler frequencies, 2) a small fraction of the direct signal being received via the side/backlobe of the receiver antenna (which is still significantly larger than the clutter echo) which masks target echo signals, and 3) strong target echoes masking other echoes from other targets of a lower level, even in the presence of large range-Doppler separations.

The masking effect due to the low peak-sidelobe level of the ambiguity function cannot be removed by conventional moving target indicator (MTI) techniques, due to the extensive range-Doppler spreading of the interference. Hence, novel adaptive cancellation filters have had to be designed for this

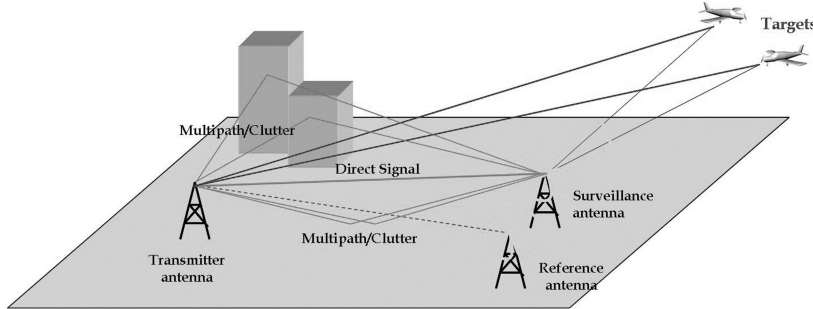


Fig. 1. PCL geometry.

purpose [4, 9–14]. In particular, this was addressed in [10] and [12] using an iterative approach that progressively cancels strong multipath and target echoes (while retaining in memory the location of the strong targets). A sequential cancellation algorithm (SCA) was presented in [14] that exploits a variable number of iterations adaptively identified from the measured data itself. The approach was designed to prioritise cancellation of the largest disturbance until a desired, predetermined, cancellation level was reached. While the ordering strategy and stopping condition proposed in [14] allows, in theory, a smart selection of the number of iterations, the application to real data is very time consuming, due to the very high possible number of degrees of freedom corresponding to a very high Doppler resolution.

In this paper, a multistage processing algorithm is presented based on the approach described in [14], but applied within a low Doppler resolution scenario, which makes it both very robust and at the same time considerably faster. Specifically the approach presented in [14] is first appropriately modified to cope with the spreading effect of the interference over the Doppler dimension. To achieve this, data is processed in short batches and subsequently recombined. This allows a wider cancellation notch in the Doppler domain thus yielding an improved removal of the disturbance together with a reduced computational load. It is also interesting to notice that the batch structure of the algorithm intrinsically allows a potential parallelization of the algorithm.

This approach is extended over consecutive stages to progressively detect the strongest delay and frequency shifted replicas of the direct signal and thence reduces their effect on the resulting “processed” received signal. This multistage version of the algorithm operates by first removing the contaminating direct signal and the strongest clutter echoes in the surveillance channel. It then detects the strongest peaks in the range-Doppler plane in order of descending signal strength. Appropriate criteria are postulated for the selection of an adequate stopping condition for this multistage detection approach. This leads to an algorithm that is very robust and progressively detects targets, including

those with weak echoes that were initially masked by ground clutter and stronger target echo sidelobes. The resulting technique is characterised by a significant improvement in the detection performance, since the joint exploitation of multiple batches and multiple stages allows both a stronger clutter/multipath cancellation (due to the short-time filter weights update) and the capability to extract some of the weak targets echoes that are likely to be lost by conventional, single stage techniques.

The effectiveness of the algorithmic approach is first demonstrated with application to simulated data, generated by a signal emulator that was developed in [8], where some targets were deliberately hidden in the sidelobes of stronger targets. Following this, the algorithms are further examined via test against a real data set recorded by an experimental FM PBR system which recorded aircraft movements over London in the UK.

Although we focus on the use of FM radio signals in this paper, it should be noted that the approach can be applied to any transmission of opportunity, such as those from cell-phone transmissions, digital radio or television waveforms, and navigation satellites. Indeed the choice of FM transmissions arguably results in waveforms with the worst ambiguity properties for target detection.

The paper is organised as follows. Section II describes the signal model and reference scenario. Section III derives a least square (LS) technique for extensive cancellation of clutter and direct signal from the received signal. Section IV introduces a batch version of this algorithm while in Section V this algorithm is extended over consecutive stages to remove the masking effect of the strong targets on the others. Also a suboptimal version of the multistage algorithm is described in Section V. In each section the performance of the algorithm is analysed with application to simulated data. In Section VI the algorithms true effectiveness is demonstrated using real data. Finally, conclusions are drawn in Section VII.

II. SIGNAL MODEL AND REFERENCE SCENARIO

A typical passive radar geometry is shown schematically in Fig. 1. For the purpose of our analysis, the reference and surveillance antennas

are assumed to be colocated with the reference antenna steered toward the transmitter and the surveillance antenna pointed in the direction to be surveyed. Next the signal model is described, paying particular attention to the representation of different contributions contained within the received signals at each receiving antenna. Due to the low frequency (UK FM radio band 88–108 MHz) used for this form of PBR, multipath and clutter are modelled as a set of small discrete scatterers. A continuous clutter backscattering environment can be emulated by utilising a large number of such ground scatterers. Based on this assumption, the complex envelope of the total signal in the surveillance channel is given by

$$s_{\text{surv}}(t) = A_{\text{surv}}d(t) + \sum_{m=1}^{N_T} a_m d(t - \tau_m) e^{j2\pi f_{dm} t} + \sum_{i=1}^{N_C} c_i d(t - \tau_{ci}) + n_{\text{surv}}(t), \quad 0 \leq t < T_0 \quad (1)$$

where

T_0 is the global observation time;

$d(t)$ is the complex envelope of the direct signal (a delayed replica of the transmitted signal);

A_{surv} is the complex amplitude of the direct signal received via the side/backlobe of the surveillance antenna;

a_m , τ_m , and f_{dm} are the complex amplitude, the delay (with respect to the direct signal) and the Doppler frequency of the m th target ($m = 1, \dots, N_T$);

c_i and τ_i are the complex amplitude and the delay (with respect to the direct signal) of the i th stationary ground scatterer ($i = 1, \dots, N_C$);

$n_{\text{surv}}(t)$ is the thermal noise contribution at the surveillance antenna.

The complex envelope of the signal at the reference channel is

$$s_{\text{ref}}(t) = A_{\text{ref}}d(t) + n_{\text{ref}}(t) \quad (2)$$

where A_{ref} is the complex amplitude and $n_{\text{ref}}(t)$ is the thermal noise contribution. Since the direct signal is received by the mainlobe of the reference antenna, it is assumed that target and clutter echoes (received from the sidelobes) are negligible. Moreover, in order to simplify the analysis, it is assumed that the reference signal is free of multipath. It is also noted that the effect of multipath on the reference channel has been analysed in [15] where possible algorithms for its removal have been introduced.

The detection process in passive radar is based on the evaluation of the delay-Doppler cross-correlation function between the surveillance and the reference signal:

$$\xi(\tau, f_D) = \int_0^{T_0} s_{\text{surv}}(t) \cdot s_{\text{ref}}^*(t - \tau) \cdot e^{-j2\pi f_D t} dt. \quad (3)$$

Assuming operation with a digital receiving system, with a sampling frequency f_s which satisfies the Nyquist theorem, the samples $s_{\text{surv}}[i]$ collected at the surveillance receiving channel at time instants $t_i = i/f_s = iT_s$, $i = 0, \dots, N - 1$, are arranged in an $N \times 1$ vector:

$$\mathbf{s}_{\text{surv}} = [s_{\text{surv}}[0], s_{\text{surv}}[1], s_{\text{surv}}[2], \dots, s_{\text{surv}}[N - 1]]^T \quad (4)$$

where N is the number of samples to be integrated. Similarly, we collect $N + R - 1$ samples of the signal from the reference channel in the following vector:

$$\mathbf{s}_{\text{ref}} = [s_{\text{ref}}[-R + 1], \dots, s_{\text{ref}}[0], \dots, s_{\text{ref}}[N - 1]]^T \quad (5)$$

where $R - 1$ is the number of additional reference signal samples to be considered in order to obtain the desired integration (namely N integrated samples) over an extent of R time bins.

Thus (6) describes the discrete implementation of a 2D cross-correlation function (2D-CCF) of (3):

$$\xi[l, p] = \sum_{i=0}^{N-1} s_{\text{surv}}[i] \cdot s_{\text{ref}}^*[i - l] \cdot e^{-j2\pi p i / N} \quad (6)$$

where

$l = 0, \dots, R - 1$ is the time bin representing the time delay $\tau[l] = lT_s$, with respect to the direct signal, of a backscattered echo at relative bistatic range $\Delta R_{\text{bis}}[l] = R_{\text{bis}}[l] - B = lT_s c$, (and B is the baseline (i.e., the distance between the Tx and the Rx) and c is the speed of light);

p is the Doppler bin representing the Doppler frequency $f_D[p] = p/(NT_s)$ of a backscattered echo from a target moving at a bistatic velocity $v_{\text{bis}}[p] = \lambda f_D[p] = c f_D[p]/f_c$ (and λ is the wavelength corresponding to the carrier frequency f_c and $v_{\text{bis}} = v_{\text{Tx}} + v_{\text{Rx}}$ where v_{Tx} and v_{Rx} are the target relative velocities with respect to the Tx and the Rx, respectively).

To evaluate the performance of the proposed processing schemes, we firstly consider a simulated scenario where signals from an FM radio transmission band (88–108 MHz) are used as waveforms of opportunity, each having a nominal bandwidth of 150 kHz. The transmitted signal is generated using the FM radio stereo signal simulator developed in [8] according to ITU regulations for Region 1.

The spectrum of the modulating signal used to generate this waveform is shown in Fig. 2 where the different contributions related to stereophonic transmissions (baseband L + R channel, pilot tone at 19 kHz, L – R channel at 38 kHz and RDS at 57 kHz) are clearly apparent. Correspondingly Fig. 3 and Fig. 4 show the spectrum and the 2D autoambiguity function ([6]) of the resultant FM signal $d(t)$ with a duration of approximately 1 s. Specifically, Fig. 4(b)–(c) show the main cuts of the 2D autoambiguity function at zero range

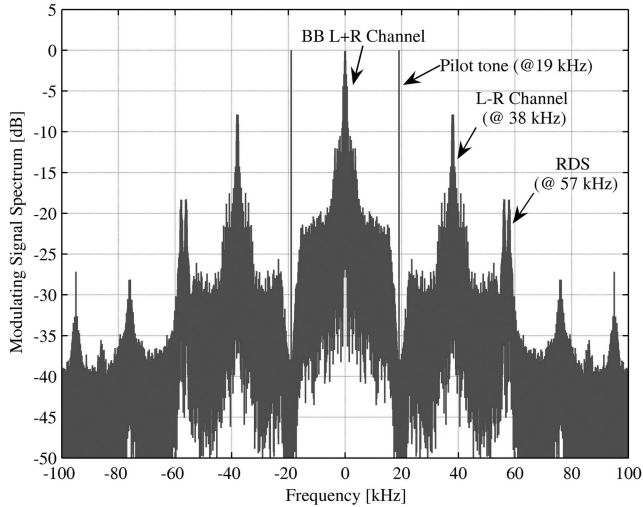


Fig. 2. Normalized spectrum of modulating signal used for simulated scenario.

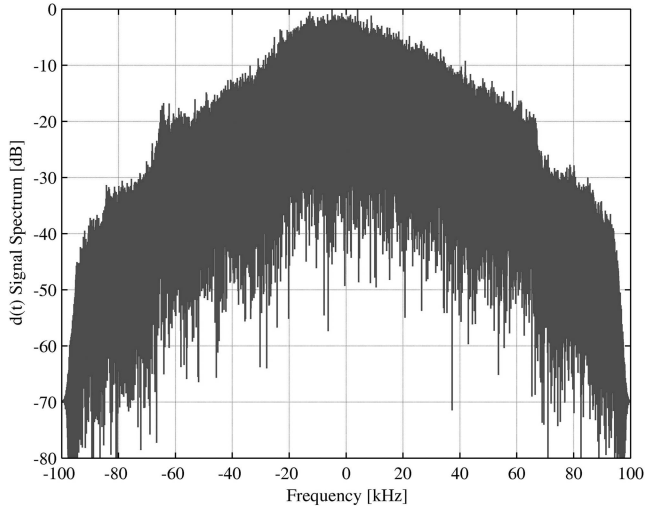


Fig. 3. Normalized spectrum of FM signal used for simulated scenario.

and zero Doppler, respectively. As is well known, the Doppler resolution achievable with an FM modulated signal is inversely proportional to the total integration time $T_{\text{int}} = NT_s$. Thus, with the aim of detecting air targets, this parameter should be selected by trading the desired integrated SNR with the expected target Doppler-range migration over the integration time. The range resolution and the sidelobe level of the exploited waveform are not within the control of the radar designer and depend on the actual transmitted radio program content. It should also be noted that, even if a nominal assigned channel bandwidth of 200 kHz is available, a typical FM radio transmission occupies a bandwidth narrower than 100 kHz thus yielding a 2-way range resolution worse than 3 km. Similarly the sidelobe level and structure is a time-varying feature which changes with the program being broadcast. The peak-to-sidelobe ratio (PSLR) of the

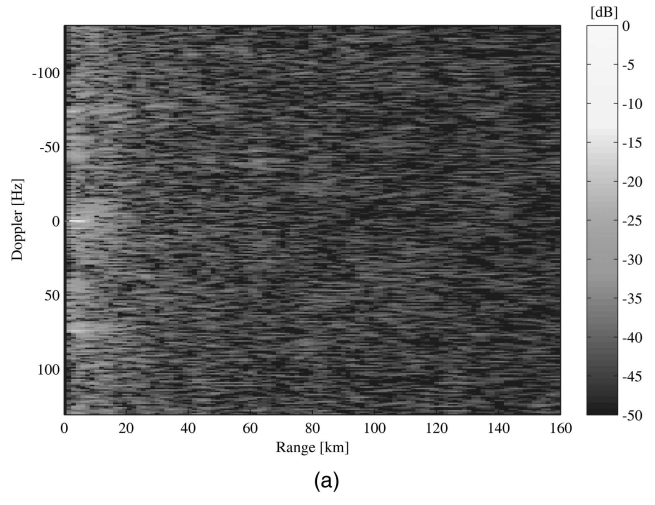


Fig. 4. 2D Autoambiguity function of FM signal used for simulated scenario. (a) 2D representation on Doppler-range plane.
(b) Zero range cut. (c) Zero Doppler cut.

autoambiguity function in Fig. 4(a) is about 18 dB which is similar to typical values measured over simulated and real data for different radio broadcasts (with the exception of the silence of course) and leads to a periodic ambiguity function. This is due to the stereo pilot tone which increases the PSLR to 0 dB [8].

TABLE I
Target Echoes Parameters for Reference Scenario

Target	#1	#2	#3	#4	#5	#6
Relative Bistatic Range (km)	20.25	60.0	60.0	99.75	110.25	129.75
Bistatic Velocity (m/s)	150	-250	50	300	-150	-300
SNR (dB)	4.1	-3.8	-20.8	-21.1	-21.6	-22.1

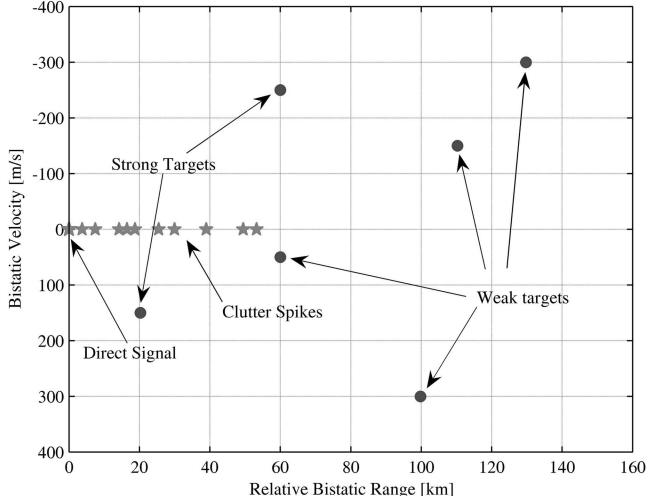


Fig. 5. Sketch of reference scenario.

An example of the range-Doppler domain considered is illustrated schematically in Fig. 5. It includes the direct signal with a direct signal-to-noise ratio (DNR) of about 63 dB and the number of scatterers $N_C = 10$. Clutter spikes can be observed with a clutter-to-noise ratio (CNR) in the range 5 dB to 35 dB in range bins between 0 km and 55 km. Six target echoes whose characteristics are listed in Table I have also been introduced. Note that bistatic range and bistatic velocity values are not directly comparable to their monostatic equivalent. Depending

on the bistatic geometry, they might need to be compared with twice their monostatic counterparts. Notice that targets 1 and 2 are labelled as “strong targets” since their SNR value is well above those of targets 3–6.

In the absence of disturbance cancellation, a strong peak corresponding to the direct signal ($\Delta R_{\text{bis}} = 0$ km and $v_{\text{bis}} = 0$ m/s) is present in the 2D-CCF. Fig. 6 shows an example for a 1 s integration time. Both the targets and the clutter spikes are completely masked by its sidelobes. Ad hoc techniques may be considered for direct signal and clutter (and multipath) removal from the surveillance signal channel to allow improved target detection. We examine one such approach in the next section.

III. EXTENSIVE CANCELLATION ALGORITHM

An effective cancellation filter for PBR can be obtained by resorting to an LS approach [14, 16]. Assuming that the multipath and clutter echoes are potentially backscattered from the first K range bins, the signal model is exploited by searching for a minimum residual signal power after cancellation of the disturbance (direct signal and ground echoes), thus:

$$\min_{\alpha} \{\|\mathbf{s}_{\text{surv}} - \mathbf{X}\alpha\|^2\} \quad (7)$$

with

$$\mathbf{X} = \mathbf{B}[\Lambda_{-P}\mathbf{S}_{\text{ref}} \cdots \Lambda_{-1}\mathbf{S}_{\text{ref}}\mathbf{S}_{\text{ref}}\Lambda_1\mathbf{S}_{\text{ref}} \cdots \Lambda_P\mathbf{S}_{\text{ref}}] \quad (8)$$

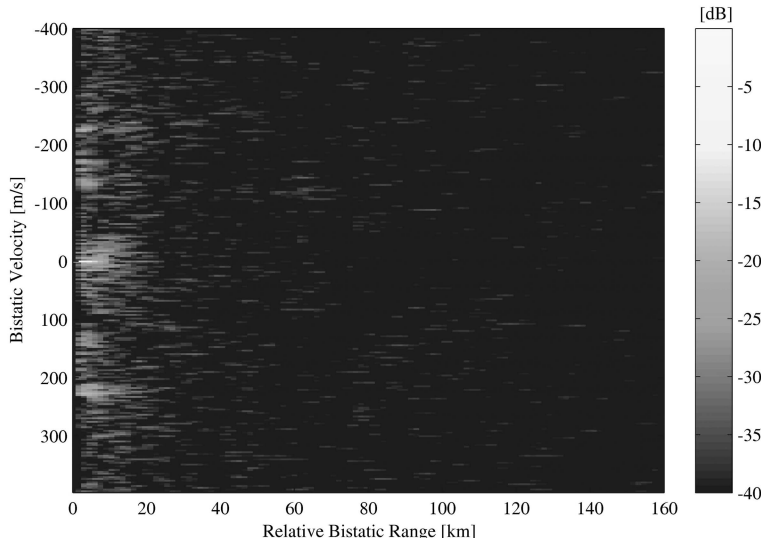


Fig. 6. 2D cross-correlation function without direct signal and disturbance cancellation.

where \mathbf{B} is an incidence matrix that selects only the last N rows of the following matrix,

$$\mathbf{B} = \{b_{ij}\}_{i=1,\dots,N, j=1,\dots,N+R-1}, \quad b_{ij} = \begin{cases} 1 & i = j - R + 1 \\ 0 & \text{otherwise} \end{cases} \quad (9)$$

Λ_p is a diagonal matrix that applies the phase shift corresponding to the p th Doppler bin:

$$\Lambda_p = \begin{bmatrix} 1 & 0 & \cdots & 0 \\ 0 & e^{j2\pi p} & \cdots & 0 \\ \vdots & \vdots & \ddots & \vdots \\ 0 & 0 & \cdots & e^{j2\pi p(N+R-1)} \end{bmatrix} \quad (10)$$

$$\mathbf{S}_{\text{ref}} = [\mathbf{s}_{\text{ref}} \quad \mathbf{D}\mathbf{s}_{\text{ref}} \quad \mathbf{D}^2\mathbf{s}_{\text{ref}} \cdots \mathbf{D}^{K-1}\mathbf{s}_{\text{ref}}] \quad (11)$$

whose columns are the zero-Doppler, delayed versions of the reference signal, and \mathbf{D} is a 0/1 permutation matrix that applies a delay of a single sample and is defined as

$$\mathbf{D} = \{d_{ij}\}_{i,j=1,\dots,N+R-1}, \quad d_{ij} = \begin{cases} 1 & i = j + 1 \\ 0 & \text{otherwise} \end{cases}. \quad (12)$$

The columns of matrix \mathbf{X} in (7) define a basis for an M -dimensional disturbance subspace, where $M = (2P + 1)K$. Solving (7) yields

$$\boldsymbol{\alpha} = (\mathbf{X}^H \mathbf{X})^{-1} \mathbf{X}^H \mathbf{s}_{\text{surv}}. \quad (13)$$

Therefore, the surveillance signal after cancellation becomes

$$\mathbf{s}_{\text{ECA}} = \mathbf{s}_{\text{surv}} - \mathbf{X}\boldsymbol{\alpha} = [\mathbf{I}_N - \mathbf{X}(\mathbf{X}^H \mathbf{X})^{-1} \mathbf{X}^H] \mathbf{s}_{\text{surv}} = \mathbf{P}\mathbf{s}_{\text{surv}} \quad (14)$$

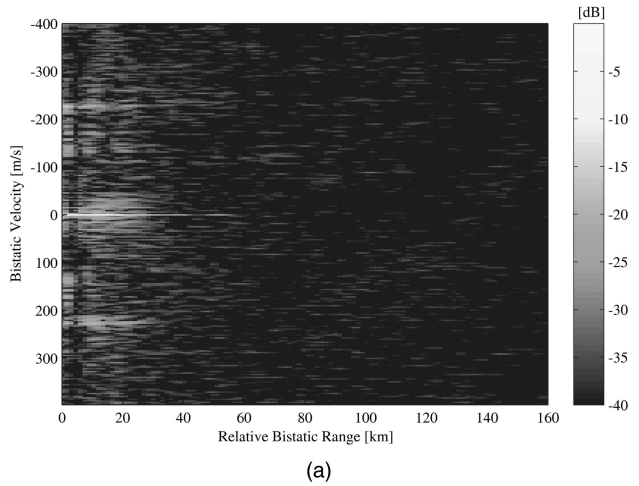
where the projection matrix \mathbf{P} projects the received vector \mathbf{s}_{surv} in the subspace orthogonal to the disturbance subspace.

The 2D-CCF evaluated at the output of the cancellation filter therefore becomes

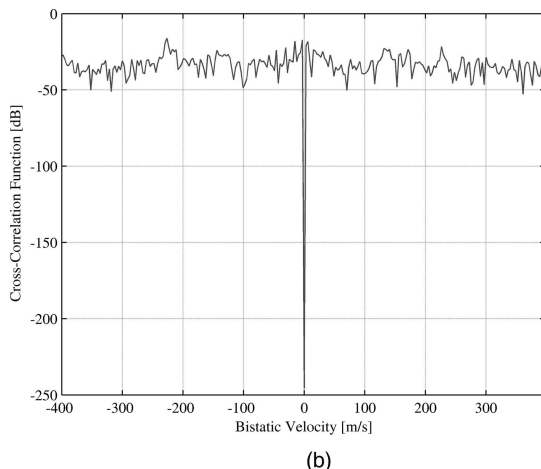
$$\xi_{\text{ECA}}[l, p] = \sum_{i=0}^{N-1} s_{\text{ECA}}[i] \cdot s_{\text{ref}}^*[i - l] \cdot e^{-j2\pi pi/N}. \quad (15)$$

Fig. 7 shows the 2D-CCF when only the direct signal is cancelled (namely $\mathbf{X} = \mathbf{B}\mathbf{s}_{\text{ref}}$ ($N \times 1$) and scalar $\boldsymbol{\alpha}$). A deep null is present at velocity zero and range zero, and the multipath/clutter spikes are quite apparent, however the targets are still not visible since they are hidden by the sidelobes of nearby ground echoes.

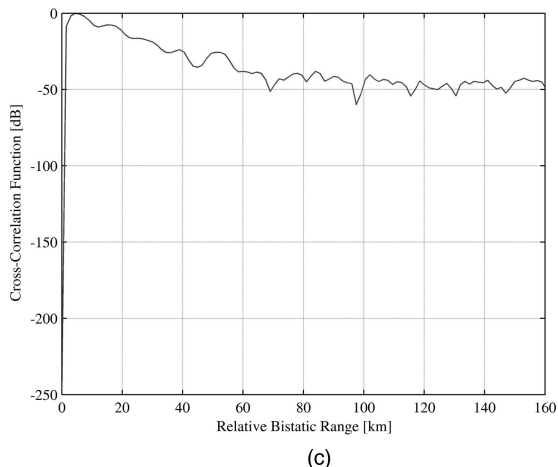
Fig. 8 shows the 2D-CCF when both the direct signal and all echoes from stationary scatterers laying in the first K range bins ($K = 50$ and $P = 0$) are cancelled (namely $\mathbf{X} = \mathbf{B}\mathbf{S}_{\text{ref}}$ of size ($N \times K$) and vector $\boldsymbol{\alpha}$ ($K \times 1$)), corresponding to a range extent of 75 km. As is apparent a deep and wide null appears at zero velocity (see Fig. 8(b)), allowing the strongest



(a)



(b)



(c)

Fig. 7. 2D cross-correlation function after direct signal cancellation with ECA. (a) 2D representation. (b) Zero range cut. (c) Zero velocity cut.

targets to be easily recognized together with their sidelobe structures.

This is confirmed in Fig. 9(a) where the result of the subsequent application of a constant false alarm rate (CFAR) threshold to the data is shown using a conventional 2D cell-averaging CFAR (CA-CFAR) algorithm with a total number of training bins equal

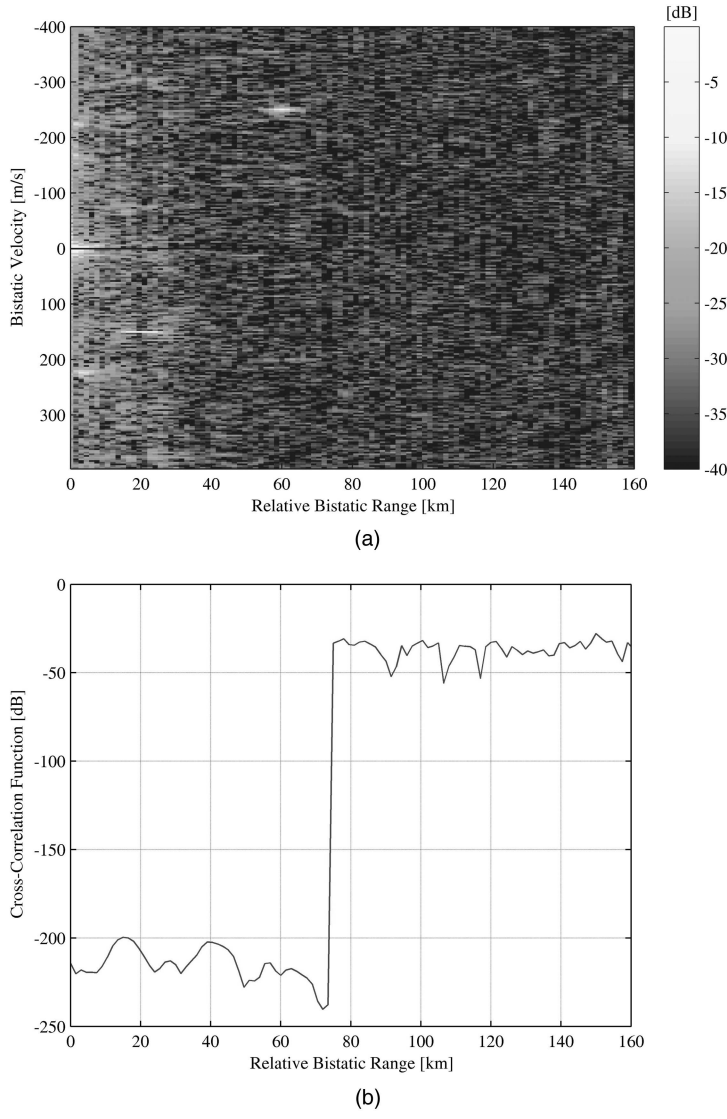


Fig. 8. 2D cross-correlation function after direct signal and ground echoes cancellation ($K = 50$, $P = 0$) with ECA.
(a) 2D representation. (b) Zero velocity cut.

to 120 and a nominal probability of false alarm, $P_{fa} = 10^{-4}$ when operating against a zero-mean Gaussian-distributed disturbance. The circles indicate the position of the injected targets: a bold line is used for correct detections while the thin line style indicates a missed detection. Only the strong targets are now correctly detected while some false alarms arise at short ranges. In Fig. 9(b) the threshold is lowered so as to obtain a nominal $P_{fa} = 10^{-3}$. It may be observed that the target detection capability is not significantly enhanced while a large number of false alarms arise.

These false alarms are mainly due to: 1) the disturbance residuals around zero Doppler which overcome the application of the cancellation filter whose parameter estimation can be greatly affected by the nonstationary behaviour of the received signal, and 2) to the sidelobe structures of the strongest targets whose level is well above that of the weak target echoes.

With respect to the first issue, a better disturbance cancellation can be achieved by extending the disturbance subspace dimension represented by the columns of matrix \mathbf{X} by including the Doppler (velocity) dimension. As an example, Fig. 10(a) shows the 2D-CCF when both the direct signal and all echoes at Doppler bins $(-1, 0, 1)$ from the first K range bins ($K = 40$ and $P = 1$, yielding $M = 120$) are cancelled (namely $\mathbf{X} = \mathbf{BS}_{ref}$ of size $(N \times M)$ and vector $\boldsymbol{\alpha}$ ($M \times 1$)). Using this filter, a deep null now appears in the 2D-CCF at velocity bins corresponding to Doppler bins $(-1, 0, 1)$ and at ranges corresponding to the first K bins. Correspondingly Fig. 10(b) reports the result of the application of the CFAR threshold with a nominal $P_{fa} = 10^{-4}$. It can be observed that 4 out of the 6 targets are now correctly detected.

This processing approach is computationally intensive, although it is possible to improve the cancellation capabilities without significantly

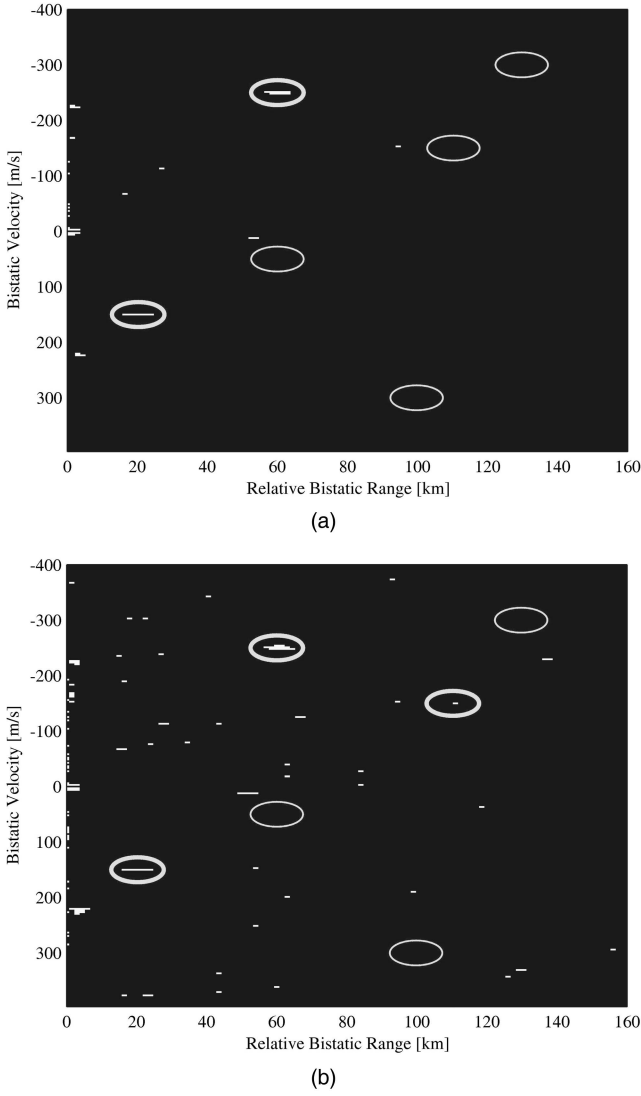


Fig. 9. Result of application of CFAR threshold on 2D-CCF of Fig. 8. (a) Nominal $P_{fa} = 10^{-4}$. (b) Nominal $P_{fa} = 10^{-3}$.

increasing the dimension of the disturbance subspace by operating over a mask of Doppler-range bins. To this purpose, the matrix $\mathbf{X} = [\mathbf{X}_0 \mathbf{X}_1 \dots \mathbf{X}_{M-1}]$ can be built by using as the i th column of \mathbf{X}_i , a proper time-delayed and Doppler-shifted replica of the reference signal according to a given mask:

$$\mathbf{X}_i = \mathbf{B} \Lambda_{p_i} \mathbf{D}^{k_i} \mathbf{s}_{\text{ref}} \quad (16)$$

where k_i and p_i represent the time and Doppler shift to be applied according to the i th bin in the mask ($i = 0, \dots, M-1$). As an example, Fig. 11 shows the 2D-CCF obtained after the application of the ECA filter operating over a mask covering 50 range bins at zero Doppler and spreading over 6 Doppler bins around zero only for the first 8 range bins ($M = 98$ bins). Almost identical detection results are obtained with respect to the previously considered case (in Fig. 10(b)) with a smaller total disturbance subspace dimensionality, yielding a lower computational load.

However, it should be noticed that in each case, despite increasing the number of degrees of freedom of the cancellation filter, the weakest injected target still cannot be correctly detected due to the sidelobes of the strongest targets. This clearly demonstrates the masking effect of the strongest targets.

However, the algorithm has the following two main limitations.

1) Its computational cost is high, since the evaluation of the weight vector α ($M \times 1$) requires the evaluation and the inversion of the matrix $\mathbf{X}^H \mathbf{X}$ with dimensions $M \times M$ which corresponds to $O[NM^2 + M^2 \log M]$ complex products.

2) It is unable to remove the masking effect of the strongest target echoes which fundamentally limits detection of the weakest targets.

In the next section modifications to the algorithm are introduced aimed at solving these limitations. In particular, a batch approach is considered in Section IV which also allows a significant reduction in the computational load while yielding similar performance. An advanced version of the algorithm is introduced in Section V which allows adaptive cancellation of the strongest target echoes in order to enable detection of the weakest ones.

IV. ECA BATCHES

In order to achieve similar or better cancellation performance with a limited computational load, a batch version of the ECA is now introduced (ECA-B). Specifically, in this approach, the ECA is applied to a set of consecutive smaller signal portions of duration T_B of the whole temporal extension T_{int} over which integration is performed. $N = T_{\text{int}} \cdot f_s$ is the number of integrated samples used for the evaluation of the 2D-CCF, the ECA algorithm is applied over b consecutive batches of $N_B = N/b$ samples each, as indicated in Fig. 12:

$$\mathbf{s}_{\text{ECA-B}} = [\bar{\mathbf{s}}_{\text{ECA}_0}^T \quad \bar{\mathbf{s}}_{\text{ECA}_1}^T \cdots \bar{\mathbf{s}}_{\text{ECA}_{b-1}}^T]^T \quad (17)$$

where

$$\bar{\mathbf{s}}_{\text{ECA}_i} = \bar{\mathbf{s}}_{\text{surv}_i} - \bar{\mathbf{X}}_i \bar{\alpha}_i \quad (18)$$

the matrix $\bar{\mathbf{X}}_i$ and the weight vector $\bar{\alpha}_i$ are evaluated using (8)–(13) where \mathbf{s}_{surv} and \mathbf{s}_{ref} are, respectively, replaced by

$$\bar{\mathbf{s}}_{\text{surv}_i} = [s_{\text{surv}}[iN_B] \quad s_{\text{surv}}[iN_B + 1] \cdots s_{\text{surv}}[(i+1)N_B - 1]]^T, \quad i = 0, \dots, b-1 \quad (19)$$

$$\bar{\mathbf{s}}_{\text{ref}_i} = [s_{\text{ref}}[iN_B - R + 1] \quad s_{\text{ref}}[iN_B - R] \cdots s_{\text{ref}}[(i+1)N_B - 1]]^T, \quad i = 0, \dots, b-1 \quad (20)$$

and N is replaced by N_B .

There are two important factors that should be taken into account.

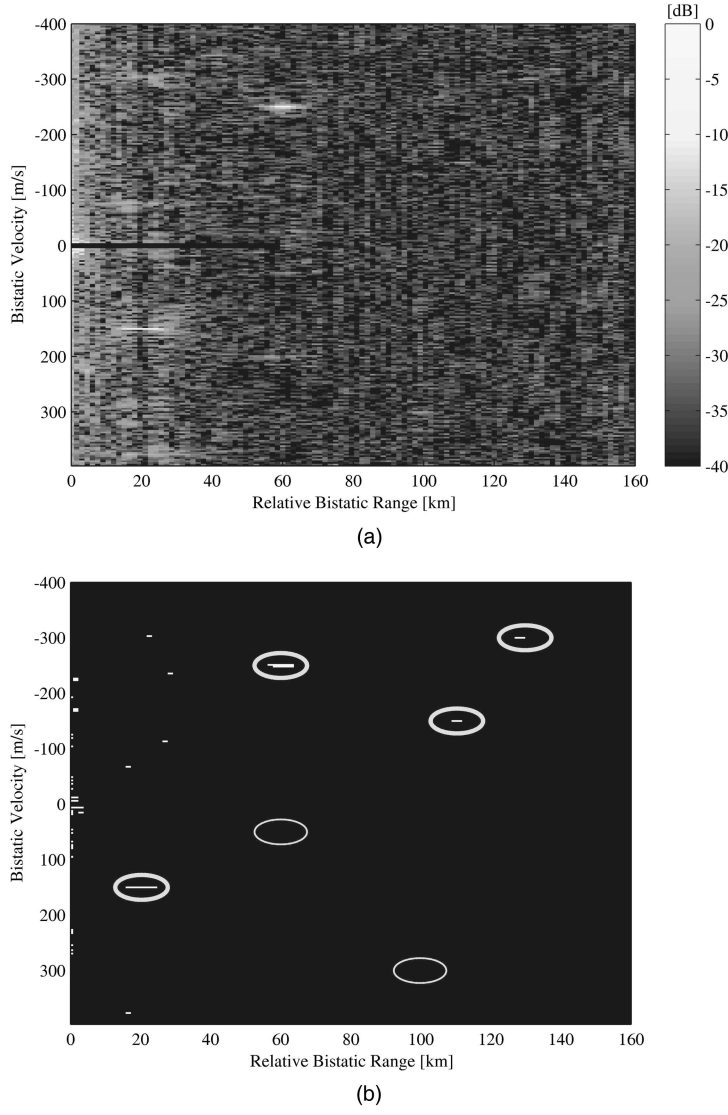


Fig. 10. Detection results after cancellation with ECA for $K = 40$ and $P = 1$ ($M = 120$). (a) 2D-CCF. (b) CFAR threshold output for $P_{\text{fa}} = 10^{-4}$.

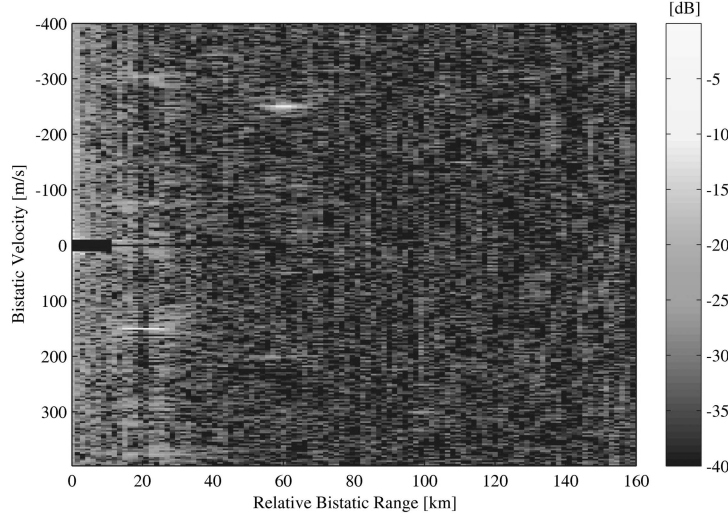


Fig. 11. 2D-CCF after cancellation with ECA with cancellation mask consisting of $M = 98$ range-Doppler bins.

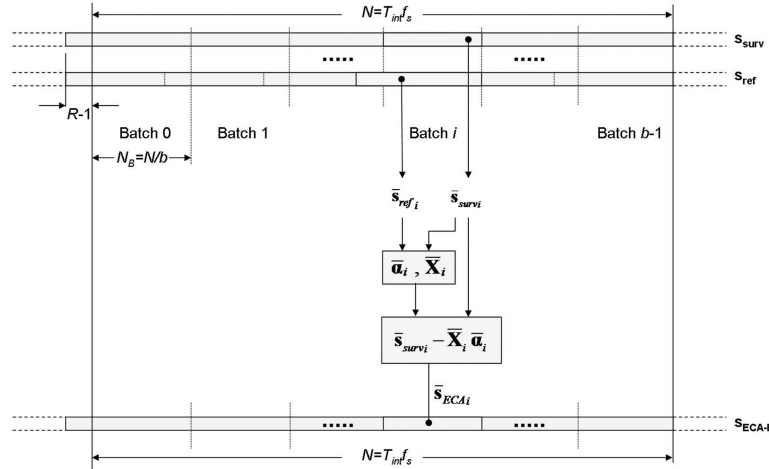


Fig. 12. Sketch of ECA-batches approach.

1) The modification of the original ECA will still require the evaluation and inversion of the matrix $\bar{\mathbf{X}}_i^H \bar{\mathbf{X}}_i$ with dimension $M \times M$, which in this case corresponds to $O[N_B M^2 + M^2 \log M]$ complex products. Clearly this computation needs to be repeated on each batch thus yielding only a limited increase in the computational burden (about the same order of magnitude in terms of complex products), namely $O[NM^2 + bM^2 \log M]$ in place of $O[NM^2 + M^2 \log M]$. However, at each batch, the dimension of the data can be reduced by a factor b thus setting a correspondingly reduced requirement on the dynamic storage capability of the system. Moreover the cancellation processing can run in parallel with the data acquisition since it can be started after samples belonging to the first batch have been received. This allows the processing rate to be lowered (which can be the limiting factor in real time applications).

2) The dimension N_B of the single batch sets the time extent over which the adaptive filter parameters are estimated. Reducing this temporal extension within certain limits does yield significant adaptivity loss when operating in a stationary environment. However, it can make the system more robust to the slowly varying characteristics of a typical radio broadcast. Moreover, operating with a temporal extent of T_B , the Doppler resolution capability of the resultant cancellation filter is degraded with respect to the ECA approach operating over the whole T_{int} period. This results in a wider notch in the Doppler dimension which has been demonstrated to be a significant feature in the previous section where this widening in the Doppler dimension was obtained at the expense of a higher computational load.

To demonstrate the potential of the ECA-B approach, it has been applied to the same set of simulated data used for the previous analyses. Fig. 13(a) shows the 2D-CCF obtained after the application of the ECA-B for $b = 10$ when both the direct signal and all echoes from stationary

scatterers laying in the first K range bins ($K = 50$ and $P = 0$) are cancelled (vector $\bar{\alpha}_i$ ($K \times 1$), $i = 0, \dots, 9$). Fig. 13(a) shows a deep null around zero bistatic velocity, thus allowing the strongest targets to be easily recognized together with their sidelobe structures. The width of the notch in the Doppler dimension is significantly increased with respect to Fig. 8(a) which was obtained with ECA operating with the same disturbance basis dimension of $M = K = 50$. It is even larger than in Fig. 10(a) where a Doppler spreading over 3 adjacent Doppler bins was considered. This effect yields a better disturbance cancellation without requiring the extension of the disturbance subspace dimension. This is confirmed in Fig. 13(b) where 4 out of the 6 targets are correctly detected. This is similar to the performance of the ECA applied with a Doppler spreading and cancellation mask (see Fig. 10(b)), with a similar number of false alarms.

Notice that, in those cases, the ECA algorithm operates with a total number of range-Doppler bins $M = 120$ and $M = 98$, respectively. Thus it is possible to assert that the ECA-B algorithm operating with a total number of range-Doppler bins $M = 50$ and $b = 10$ batches yields similar performance with a computational load saving factor of approximately 6 and 4, respectively. It is to be noted that for real-time operation, a proper implementation of this technique should be selected, that considers the equivalent solution of the least mean square (LMS) problem based on the use of the Householder triangularization. In addition, the ECA-B algorithm can be applied over a proper mask in the Doppler-range plane. However, as in the case of the ECA, the mask definition requires certain a degree of a priori knowledge about the form of the disturbance power as it spreads over the Doppler-range plane.

It should also be noted that the detection of the weakest targets is no longer limited by residuals of the cancellation process but by the masking effect of the sidelobes of the strongest targets. It is then

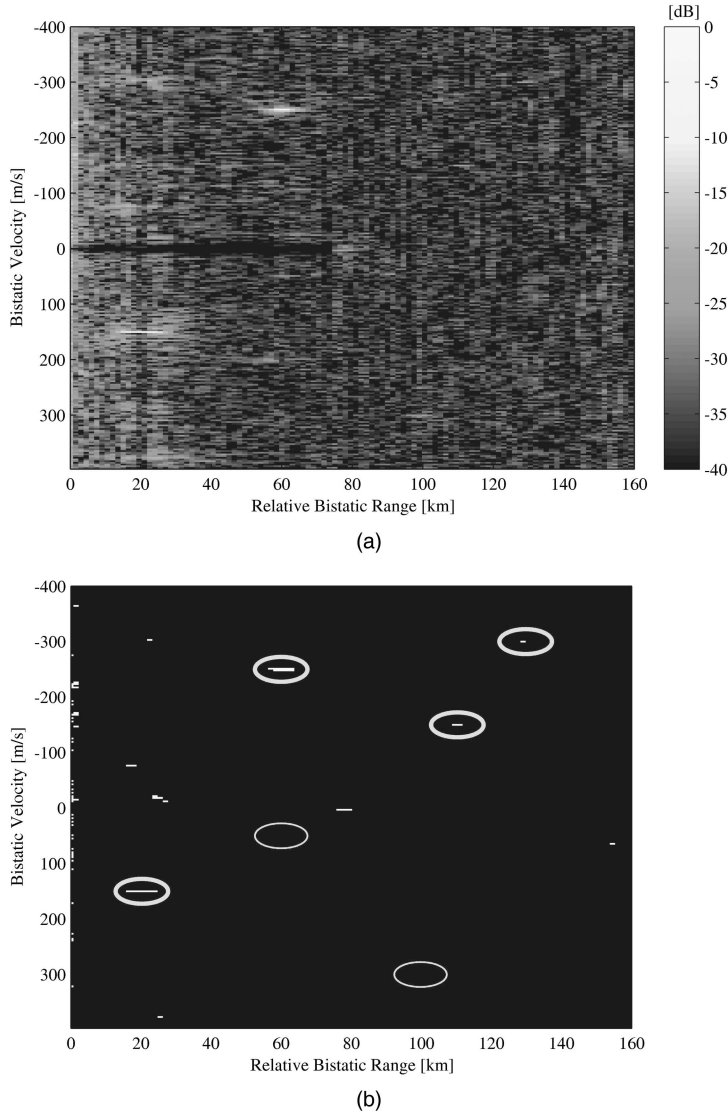


Fig. 13. Detection results after cancellation with ECA-B for $b = 10$, $K = 50$, and $P = 0$. (a) 2D-CCF. (b) CFAR threshold output for $P_{fa} = 10^{-4}$.

useless to further increase the dimensionality of the disturbance subspace while the degrees of freedom saved by using the ECA-B approach can be devoted to counteract this new limitation. To this purpose, an ad hoc algorithm has been developed and is now presented in the following section. It is based on the ECA-B and yields additional capability by removing the strongest targets thus allowing the detection of the weakest ones as well.

V. ECA BATCHES & STAGES

In this section a complete processing algorithm is presented based on the ECA-B approach which allows:

- 1) a preliminary cancellation of the main disturbance contributions,
- 2) a cancellation performance refinement by the adaptive definition of an extended cancellation mask,

3) the removal of the strongest targets thus yielding the detection of the weakest ones.

A. Algorithm Description

This development of the algorithmic approach uses multiple consecutive stages of the ECA-B (ECA-B&S—ECA batches & stages). The main steps are illustrated in Fig. 14 and are described as follows.

- 1) The ECA-B algorithm is first applied over a range extent including K range bins and $P = 0$ (no Doppler spread) and the corresponding 2D-CCF is evaluated. This first step yields nearly complete cancellation of the disturbance contributions (i.e., direct signal and ground clutter). As previously demonstrated, after this step the disturbance residual power and the strongest targets clearly appear as strong peaks in the 2D map, together with their sidelobe structures.

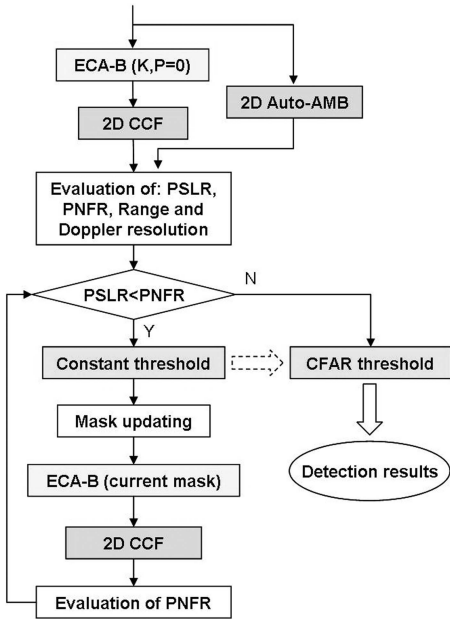


Fig. 14. ECA-batches & stages flow diagram.

2) The 2D autoambiguity function of the reference signal is evaluated which gives information about 1) range and Doppler resolution, and 2) the sidelobe level in terms of PSLR. At the same time, using the 2D-CCF, the actual noise floor is estimated over a small portion of the Doppler-range surface at high values, where no target is expected to fall and the effects of the waveform (lobes main structures) may be assumed negligible. Specifically the peak-to-noise-floor ratio (PNFR) is evaluated, between the main peak of the 2D-CCF and the estimated noise floor.

3) The PNFR is compared with the PSLR. If the PNFR is smaller than the PSLR, it means that the strongest targets' sidelobes are buried in the noise floor and target detection is only limited by the latter. In this case, a CFAR threshold is applied over the 2D-CCF as described in the previous sections for a given nominal P_{fa} and the algorithm stops. In fact, upon arrival at this stage no better target extraction can be expected by further removing detections. Notice that in this case, the ECA-B&S coincides with the ECA-B with the exception of the additional evaluation of the 2D autoambiguity function at step 2.

4) If the PNFR is higher than the PSLR, a constant threshold is applied on the 2D-CCF of step 1. This threshold is set at η dB below the main peak of the 2D-CCF, η being a given value in the range $[0, \text{PSLR}]$ dB. This allows detection of the strongest peaks in the Doppler-range plane which are due to disturbance residuals and strong targets, while avoiding false alarms from sidelobes. Notice that most of the detections associated with disturbance residuals usually appear at very short ranges and can be discarded at a postprocessing stage. The detected

target positions are stored in order to be added to the final detection results in a later stage.

5) The Doppler-range bins at which a detection was declared in step 4 are used to update the cancellation mask and a new stage of ECA-B is performed over the extended basis (which is likely to include the main contributions still limiting the detection of the smaller targets). To obtain an effective cancellation of the strongest peaks, a small area around the corresponding Doppler and range bins is considered for cancellation. The Doppler and range extents can be set adaptively using the resolution values evaluated at step 2. Subsequently, the resulting 2D-CCF is evaluated and the PNFR value is updated.

6) Steps 3–4 and 5 are repeated until the algorithm stops. Notice that, as the number of stages increases, the dimension of the mask over which cancellation is performed grows. As a consequence, the PNFR decreases for two reasons. First, the strongest peaks present in the 2D-CCF at the previous stage have been removed, thus the actual main peak has a lower absolute value. Second, the noise floor level increases slightly since a thermal noise contribution is added to the output data that comes from the reference signal replicas used for cancellation.

This algorithm has a higher computational load than the simpler ECA-B approach since it requires additional stages to achieve an effective removal of the interference contributions. However, it allows a reduction in the initial basis dimension of the cancellation algorithm, since the cancellation mask is adaptively updated. Thus it avoids making the number of degrees of freedom of the filter too great.

The common threshold at step 4 should be set according to the number of strong targets that are expected. In fact lowering η yields a bigger number of stages since only few targets are removed at each stage. However, as η increases, a higher number of targets can be detected at each stage and the cancellation mask can rapidly increase. Moreover, the sidelobe structures of the strongest targets can partially overlap thus yielding higher values with respect to those obtained from the PSLR measured on the autoambiguity function of the reference signal. As a consequence, the η value should always be smaller than the PSLR.

The algorithm stop condition is described at step 3. As apparent, it requires the estimation of the noise floor which is obtained from the current 2D-CCF. Also in this case, in order to prevent additional stages due to noise floor estimation inaccuracy, a more conservative stop condition can be used by comparing $\text{PNFR}_{\text{dB}} \geq \text{PSLR}_{\text{dB}} + \varepsilon_{\text{dB}}$. Last, an additional stop condition can be used based on the maximum allowable cancellation mask dimension.

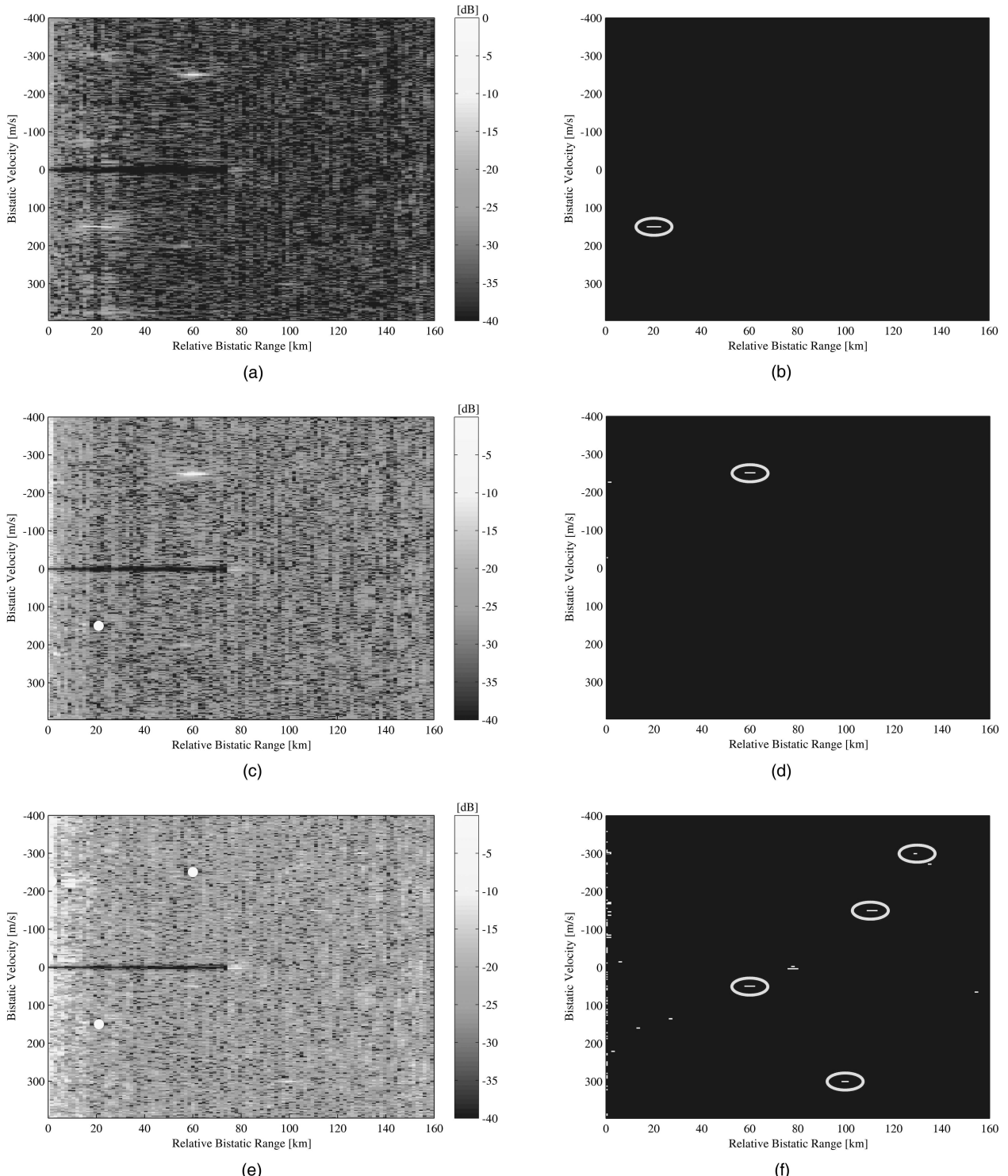


Fig. 15. Results of ECA-B&S algorithm with parameters listed in Table II. (a)–(c)–(e) 2D-CCF after stages 1–2–3. (b)–(d)–(f) detection results after stages 1–2–3.

TABLE II
ECA-B&S Parameters for Simulated Data Processing

number of batches b	10
initial $M = K$ ($P = 0$)	50
ε	3 dB
η	5 dB
P_{fa} (for the CFAR threshold)	10^{-5}

B. Performance Analysis for the Reference Scenario

The ECA-B&S is now applied to the simulated data set used in the previous sections, with the operating parameters listed in Table II. The algorithm stops after 3 stages. The results obtained at each stage are shown in Fig. 15.

In particular Fig. 15(a) shows the 2D-CCF after the first stage of the algorithm which coincides with that reported in Fig. 13(a) for the ECA-B approach operating on the same number of range bins. The reference signal autoambiguity PSLR is 18.2 dB while the estimated PNFR is 33.5 dB, thus a constant threshold is applied giving the result shown in Fig. 15(b). As apparent only the strongest target is detected, whose position is used to update the cancellation mask for the following stage. The Doppler and range resolutions of the exploited waveform suggest consideration of a cancellation area around the target position with an extension of 1 bin in the velocity dimension and 5 bins in the range dimension. Thus the updated mask to be used in the following stage is made up of $M = 50 + 5$ bins.

Fig. 15(c) shows the 2D-CCF after the second stage of the algorithm. A red circle is used to indicate the position of the previously detected target. It is apparent that the strongest target has been correctly removed together with its sidelobes and the second strongest target now appears as the strongest peak. Also the weak targets show up, however it is still difficult to discriminate them from the background. The updated value of the PNFL is 25.0 dB which is still higher than the PSLR and a constant threshold is again used with the results reported in Fig. 15(d). In this case the second strongest target is detected together with some disturbance residuals at very short ranges.

The new updated cancellation mask includes $M = 67$ bins and the 2D-CCF obtained after using this new mask is shown in Fig. 15(e). Notice that all the 2D-CCFs are normalized to their peak value, and in this case the dynamic range is clearly limited by thermal noise. In fact the new estimated PNLR is 19.5 dB which is only $1.3 \text{ dB} < \varepsilon|_{\text{dB}}$ above the PSLR value. Thus the CFAR threshold approach is used giving the results shown in Fig. 15(f). As is apparent all the four weak targets are correctly detected even though a smaller cancellation filter basis dimension and a higher threshold have been used compared with the examples analysed in the previous sections.

C. Implementation of the ECA-B&S

The described approach yields better detection capabilities with respect to the simpler versions of the ECA and ECA-B. This is paid for in terms of high computational load since different cancellation stages are required and the basis of the disturbance space is extended at each stage, including the subspace spanned by the strongest target returns.

To counteract this problem a suboptimal implementation of the ECA-B&S is introduced. The suboptimal implementation of the algorithm performs a cancellation, at each stage, which only involves the small subspace spanned by the strongest targets

detected at the previous stage. This corresponds to an assumption that this subspace is orthogonal to the subspace spanned by the disturbance basis used in the previous stage, for example.

The output of the cancellation filter after the first stage is given by

$$\bar{\mathbf{s}}_{\text{ECA-B\&S}}^{(I)} = [\bar{\mathbf{s}}_{\text{ECA}_0}^T \quad \bar{\mathbf{s}}_{\text{ECA}_1}^T \cdots \bar{\mathbf{s}}_{\text{ECA}_{b-1}}^T]^T \quad (21)$$

where

$$\begin{aligned} \bar{\mathbf{s}}_{\text{ECA}_i}^{(I)} &= \bar{\mathbf{s}}_{\text{surv}_i} - \bar{\mathbf{X}}_i^{(I)} \bar{\alpha}_i^{(I)} \\ &= [\mathbf{I} - \bar{\mathbf{X}}_i^{(I)} (\bar{\mathbf{X}}_i^{(I)H} \bar{\mathbf{X}}_i^{(I)})^{-1} \bar{\mathbf{X}}_i^{(I)H}] \bar{\mathbf{s}}_{\text{surv}_i} = \mathbf{P}_i^{(I)} \bar{\mathbf{s}}_{\text{surv}_i} \end{aligned} \quad (22)$$

and the matrix $\bar{\mathbf{X}}_i^{(I)}$ and the weight vector $\bar{\alpha}_i^{(I)}$ are evaluated using (8)–(13) where $\bar{\mathbf{s}}_{\text{surv}_i}$ and $\bar{\mathbf{s}}_{\text{ref}_i}$ are defined in (19)–(20), respectively. The projection matrix $\mathbf{P}_i^{(I)}$ projects the vector $\bar{\mathbf{s}}_{\text{surv}_i}$ in the subspace orthogonal to the disturbance subspace considered at the first stage. Clearly, (21) coincides with (17) for the ECA-B if the same initial mask is used at the first stage of the ECA-B&S algorithm.

The matrix $\bar{\mathbf{X}}_i^{(II)}$ that is to be used at the second stage of the ECA-B&S is given by

$$\bar{\mathbf{X}}_i^{(II)} = [\bar{\mathbf{X}}_i^{(I)} \bar{\mathbf{T}}_i^{(I)}] \quad (23)$$

where the columns of $\bar{\mathbf{T}}_i^{(I)}$ are time delayed and Doppler shifted replicas of $\bar{\mathbf{s}}_{\text{ref}_i}$ which define a basis for the subspace spanned by the strong targets detected at the first stage. Therefore, the single batch output after the second cancellation stage is given by

$$\begin{aligned} \bar{\mathbf{s}}_{\text{ECA}_i}^{(II)} &= \bar{\mathbf{s}}_{\text{surv}_i} - \bar{\mathbf{X}}_i^{(II)} \bar{\alpha}_i^{(II)} \\ &= [\mathbf{I} - \bar{\mathbf{X}}_i^{(II)} (\bar{\mathbf{X}}_i^{(II)H} \bar{\mathbf{X}}_i^{(II)})^{-1} \bar{\mathbf{X}}_i^{(II)H}] \bar{\mathbf{s}}_{\text{surv}_i} = \mathbf{P}_i^{(II)} \bar{\mathbf{s}}_{\text{surv}_i} \end{aligned} \quad (24)$$

where the projection matrix $\mathbf{P}_i^{(II)}$ projects the vector $\bar{\mathbf{s}}_{\text{surv}_i}$ in the subspace orthogonal to the subspace spanned by the columns of $\bar{\mathbf{X}}_i^{(II)}$. To proceed further, we define the projector $\mathbf{P}_{Ti}^{(II)}$ as

$$\mathbf{P}_{Ti}^{(II)} = \mathbf{I} - \bar{\mathbf{T}}_i^{(I)} (\bar{\mathbf{T}}_i^{(I)H} \bar{\mathbf{T}}_i^{(I)})^{-1} \bar{\mathbf{T}}_i^{(I)H}. \quad (25)$$

Assuming that the subspace spanned by the columns of $\bar{\mathbf{T}}_i^{(I)}$ is already orthogonal to the subspace spanned by the columns of $\bar{\mathbf{X}}_i^{(I)}$ (although this is not strictly true), (24) can be rewritten as

$$\bar{\mathbf{s}}_{\text{ECA}_i}^{(II)} = \mathbf{P}_i^{(II)} \bar{\mathbf{s}}_{\text{surv}_i} = \mathbf{P}_{Ti}^{(II)} \mathbf{P}_i^{(I)} \bar{\mathbf{s}}_{\text{surv}_i} = \mathbf{P}_{Ti}^{(II)} \bar{\mathbf{s}}_{\text{ECA}_i}^{(I)}. \quad (26)$$

Since the two subspaces above are not exactly orthogonal, the use of (26) leads to a suboptimal implementation of the ECA-B&S algorithm. This only requires application of a new stage of cancellation to the output of the previous stage and uses only a small

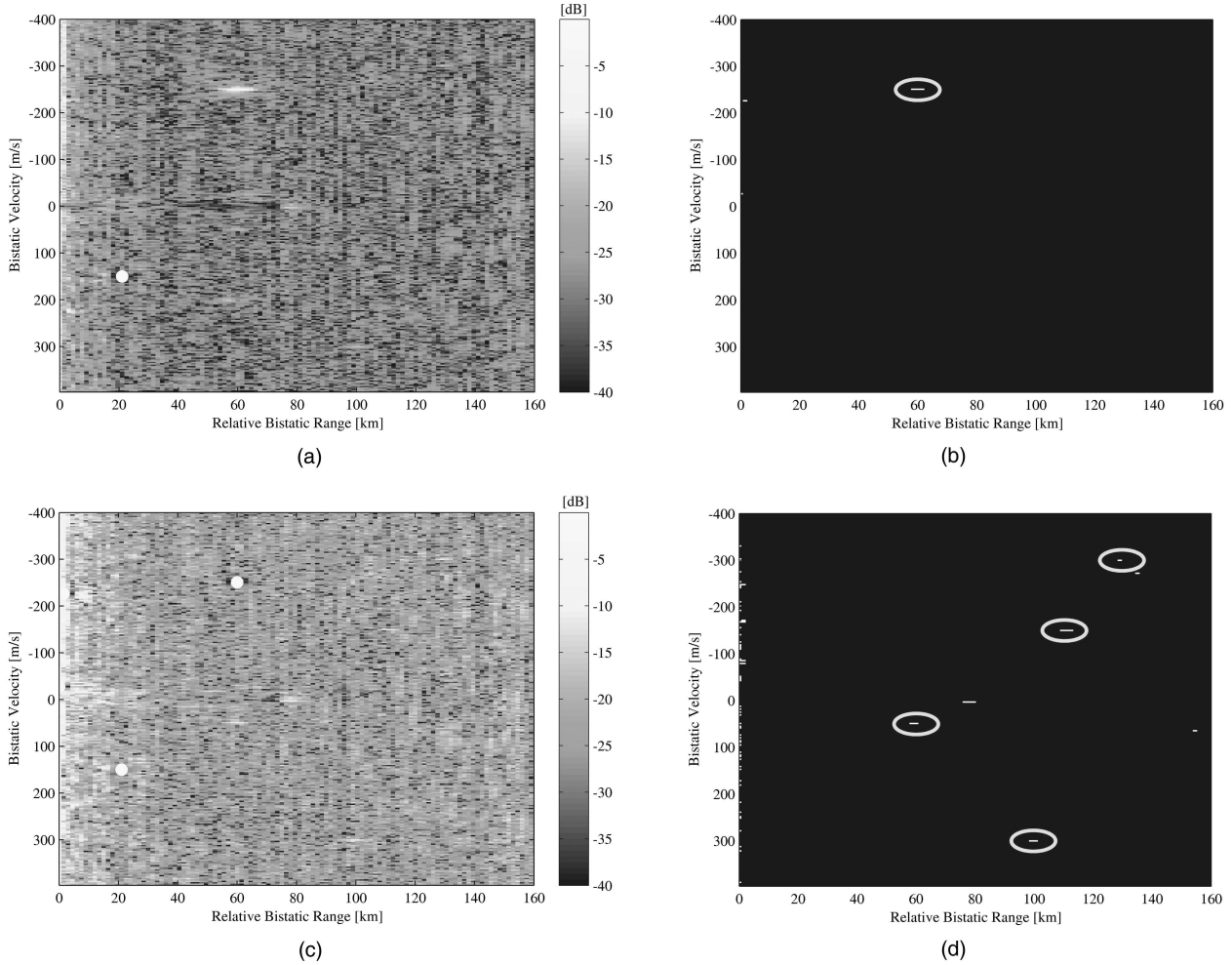


Fig. 16. Results of ECA-B&S algorithm with suboptimal implementation and parameters listed in Table II. (a)–(c) 2D-CCF after stages 2–3. (b)–(d) detection results after stages 2–3.

mask defined by the targets detected in the previous stage.

The results obtained with this version of the ECA-B&S algorithm when applied to the simulated data set are shown in Fig. 16. Specifically only the results at stages 2 and 3 are shown since the first stage of the processing is the same as that of the two previous versions. Notice that the deep notches in the 2D-CCF due to the previous stages cancellation processing disappear even when the main disturbance contributions have been removed. This shows that the hypothesis of orthogonality of the subspaces sequentially considered for cancellation is not completely satisfied. Nevertheless, this version of the algorithm yields comparable detection performance with respect to its optimal implementation. Importantly though, the computational load has been dramatically reduced. Specifically, the first stage yields the same computational burden in the two versions of the algorithm; while after N_s stages, a computational load saving of about $[(N_s M + \sum_{i=1}^{N_s-1} (N_s - i) T_i) / (M + \sum_{i=1}^{N_s-1} T_i)]^2$ is obtained using the suboptimal implementation of the ECA-B&S,

where M is the number of bins used for cancellation at the first stage, and T_i is the number of bins used for the removal of the strong targets detected at the i th stage.

VI. RESULTS ON REAL DATA

In this section the effectiveness of the above processing algorithms are demonstrated using a real data set derived from an experimental PBR system. The PBR is a prototype and operates in the [88–108] MHz frequency band. The design is based on the direct IF sampling approach described in [17]. The design is shown in Fig. 17 and is based on the use of a high quality dual channel A/D converter with a 14 bit resolution and an input bandwidth of 200 MHz. By appropriately selecting the sampling frequency of the A/D converter via an external but tunable oscillator, the ADC replicates the 20 MHz input signal satisfying the Nyquist criteria. With this approach the baseband replica of the whole [88–108] MHz frequency bandwidth is achieved. The acquired data is stored and processed off-line

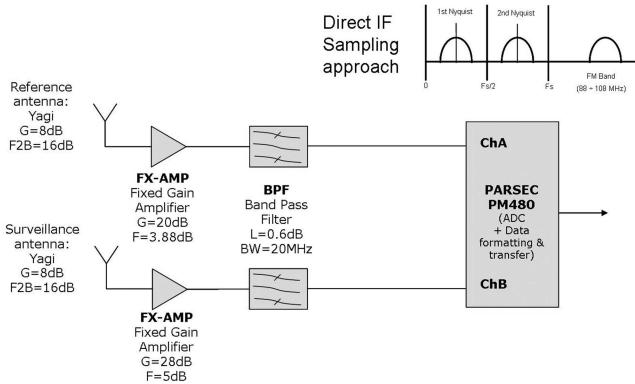


Fig. 17. Experimental receiving system.

using digital filters designed to extract the single FM channels of interest.

The data collection geometry is shown schematically in Fig. 18(a). The reference antenna was steered towards a transmitter located at Wrotham (approximately 37 km South-East of UCL) while the surveillance antenna was pointed approximately toward North-West. Both antennas are of a logarithmic design and cover the whole FM band with a beamwidth of about 100° , a gain of 8 dB and a nominal front-to-back ratio of 16 dB. They are installed on opposite sides of the building at UCL as illustrated in Fig. 18(b) to increase the direct signal rejection in the surveillance channel. Due to the large antenna beamwidth, many of the standard departure and arrival routes for Heathrow, Luton, Stanstead, and City airports are contained within the 3 dB surveillance antenna pattern.

To examine the processing algorithms, a sequence of six data acquisitions displaced by 10 s and each lasting approximately 1 s is used. For the purposes of evaluating the algorithms, the 91.3 MHz FM radio channel (BBC Radio 3) was employed. The six acquisitions contain mainly a stereophonic classical music program. As an example, Fig. 19 displays the waveform for the reference signals extracted from the first and third files of the sequence in terms of the modulating signal spectrum, the complex envelope spectrum, and the 2D autoambiguity function.

Five out of the six files show features similar to those of the first file which contains music for all the acquisition duration with an acceptable signal bandwidth (see Fig. 19(a), (c)). Notice that the obtained plots for the real signals are very similar to those of the simulated data, which confirms the effectiveness of the developed signal emulator for analysis purposes. However in the simulated case a piece of rock music was used, thus yielding a slightly better range resolution (see Fig. 19(e)).

On the contrary, the third file of the acquisitions sequence contains the end of a piece of music followed by silence. This yields a modulating signal spectrum which is dominated by the 19 kHz pilot tone

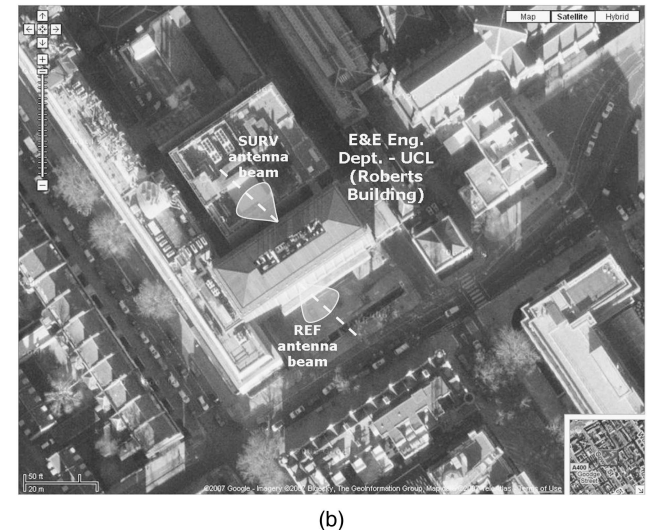
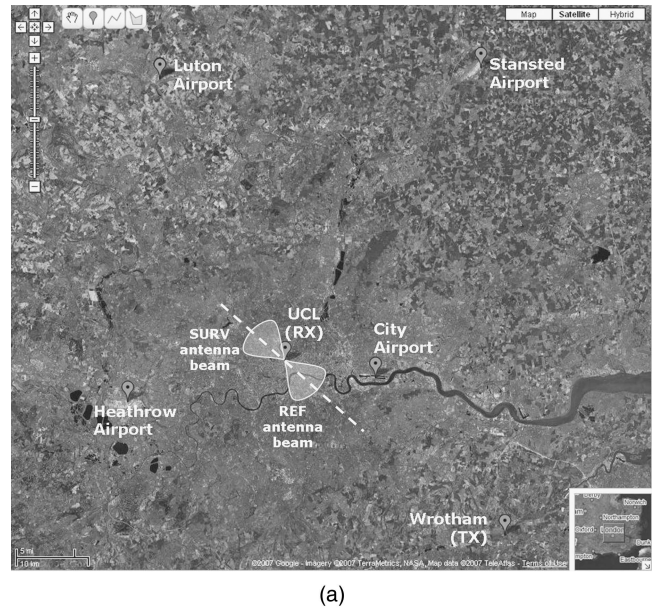


Fig. 18. Acquisition geometry. (a) Overall view. (b) Receiving system area.

component (see Fig. 19(b), (d)) which in turn results in an even further degraded range resolution and a periodic behaviour of the correspondent waveform autoambiguity function (see Fig. 19(f)), [8].

The algorithms introduced in the previous sections are now applied over all the available data files in the sequence. Fig. 20(a) shows the 2D-CCF over the fourth file after the application of the ECA with $K = 50$ and $P = 0$. As expected, a deep and wide null appears at velocity zero, thus allowing a strong target to be easily recognized together with its sidelobe structure. This is confirmed in Fig. 20(b) where the result of the application of the CFAR threshold to the data is shown ($P_{fa} = 10^{-4}$). The figure shows that only four of the possible targets are detected. As in the simulated case, even if significant direct signal cancellation has been obtained, target detection is strongly limited by the disturbance residuals around

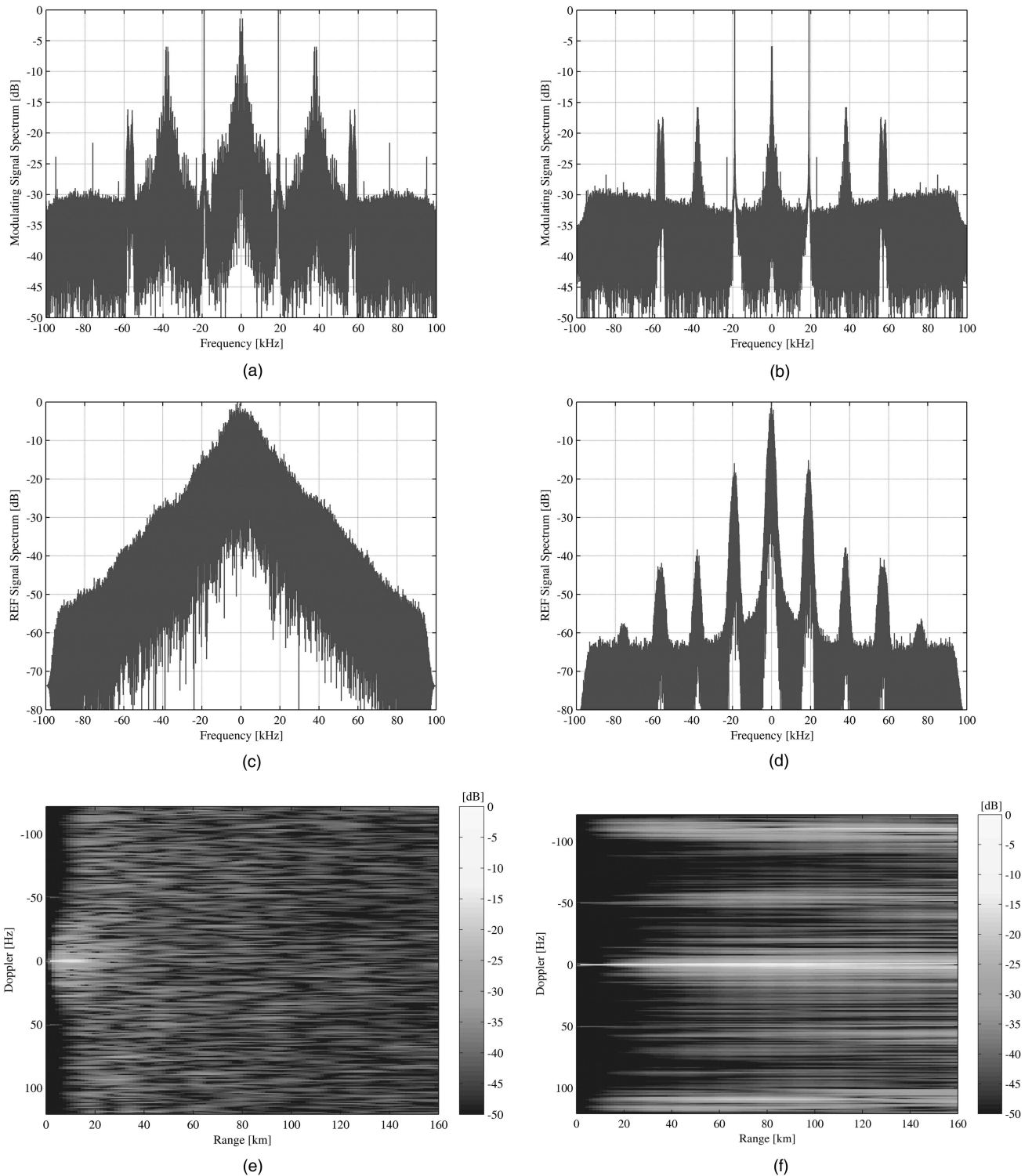


Fig. 19. Reference signal characteristics for files I and III of acquisitions sequence. (a)–(b) Modulating signals spectra for files I and III. (c)–(d) Complex envelope spectra for files I and III. (e)–(f) 2D autoambiguity functions for files I and III.

zero Doppler and by the sidelobes from the strongest targets.

Fig. 21(a)–(b) show the 2D-CCF and the detection results obtained for the same data after the application of the ECA-B for $b = 10$, $K = 50$, and $P = 0$. This clearly demonstrates the benefits, in a real case, of the wider notch in the Doppler dimension which

allows a better cancellation of the disturbance, without requiring extension of the disturbance subspace dimension. Moreover this yields improved detection performance since targets are now detected at bistatic ranges greater than 120 km.

Lastly, Fig. 22 shows the results obtained for the fourth data file at the different stages of the

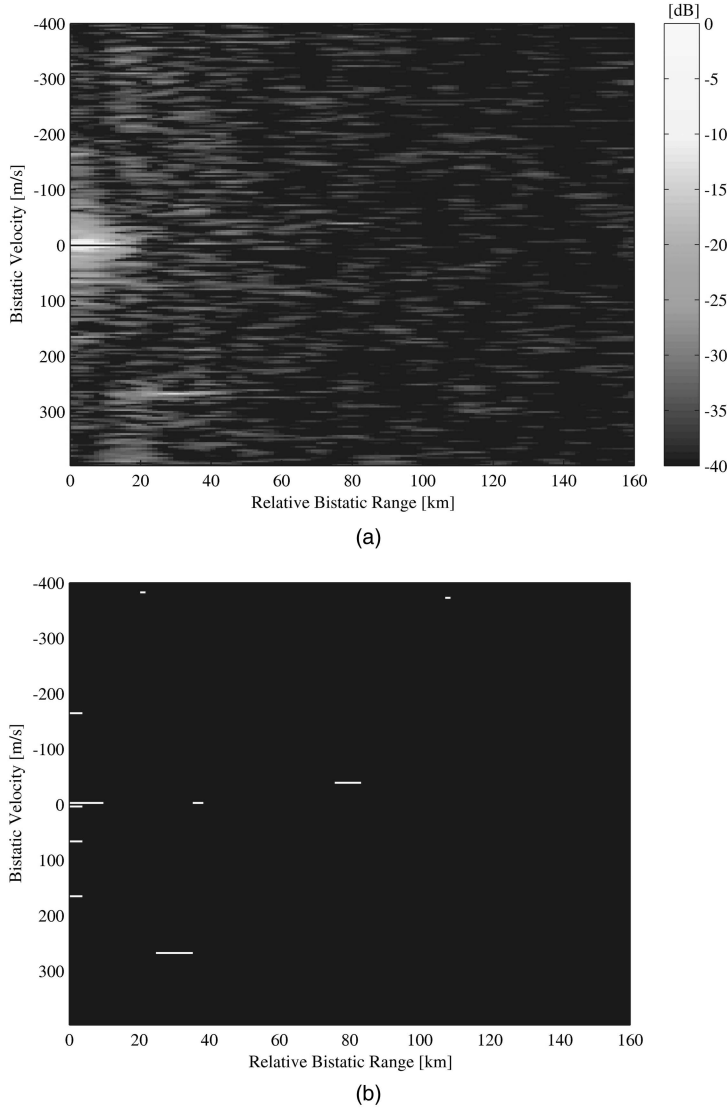


Fig. 20. Detection results for fourth file of real data set after cancellation with ECA for $K = 50$ and $P = 0$. (a) Shows 2D-CFF. (b) Shows CFAR threshold output for $P_{fa} = 10^{-4}$.

ECA-B&S algorithm (using the parameters listed in Table II and a nominal $P_{fa} = 10^{-4}$).

Three stages of cancellation are performed.

At each stage the cancellation mask is adaptively extended by adding the bins at which a peak in the 2D-CFF was found. Specifically, the reference signal autoambiguity PSLR is 24 dB while the estimated PNFR at the first stage is 35.5 dB, thus a constant threshold is applied which detects the strong target. At the second stage the estimated PNFR is 32.2 dB and the constant threshold applied over the 2D map results in many detections, probably related to disturbance residuals as they are at relative bistatic ranges smaller than 2 km. After the third stage the PNFR decreases to 26.6 dB and the detection results obtained after the application of the CFAR threshold show an increased number of detections with bistatic ranges of up to 150 km.

Fig. 23(a)–(b) shows the superposition of the detection results obtained with ECA, ECA-B, and ECA-B&S on the fourth and fifth files of the acquisition sequence, respectively. Notice that all the plots within a relative bistatic range of 5 km have been discarded assuming that they are due to disturbance residuals. The strong target at a bistatic range of 30 km and bistatic velocity of approximately 260 m/s is correctly detected by all the algorithms while only the ECA-B and ECA-B&S are able to detect other potential targets. Notice also that ECA-B&S yields additional detections with respect to ECA-B that may either be real targets or false alarms.

Fig. 24(a)–(c) shows the sequence of the detection results obtained from the six data files using the same range-Doppler map for the three algorithms. A plot sequence can be easily recognised as belonging to a possible target by observing that an approaching target has a positive bistatic velocity and the range

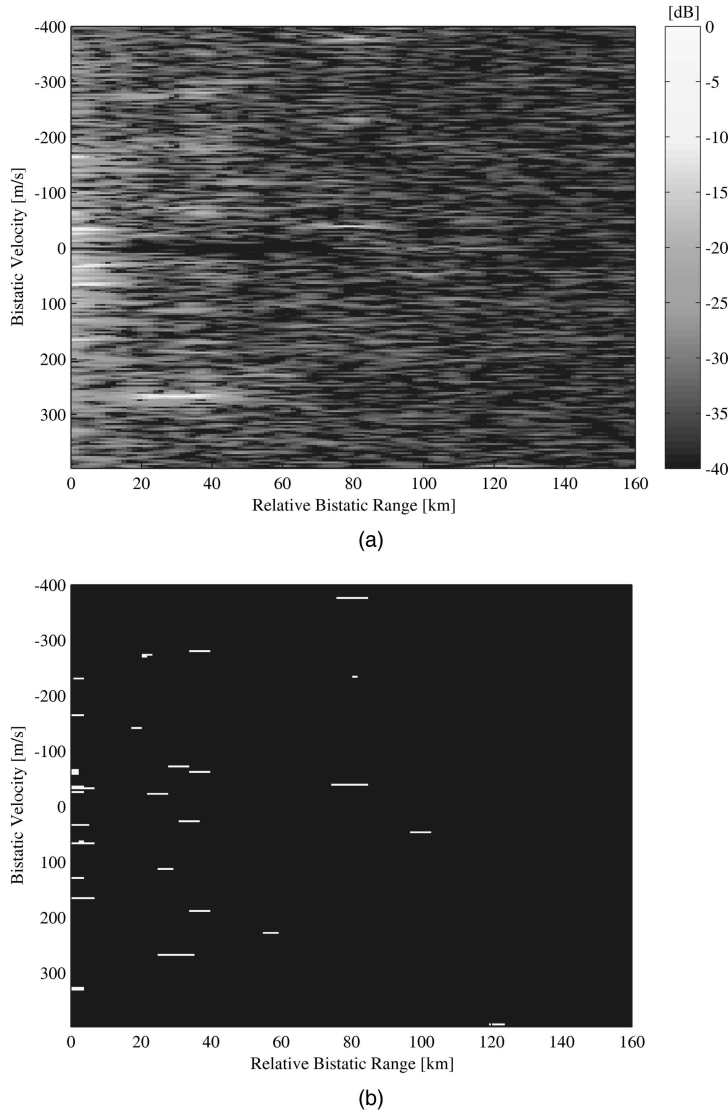


Fig. 21. Detection results for fourth file of real data set after cancellation with ECA-B for $b = 10$, $K = 50$, and $P = 0$.
(a) Shows 2D-CCF. (b) Shows CFAR threshold output for $P_{fa} = 10^{-4}$.

rate of change is directly related to the magnitude of the bistatic velocity. In each figure, the identified plot sequences are indicated with circles using different line styles according with the following criterion: the continuous bold line is for sequences containing 5/6 plots, the continuous thin line is for sequences containing 4 plots, the discontinuous black is for those containing only 3 plots, and the discontinuous grey is for possible sequences made of 2 plots.

It is apparent that, when using the ECA (Fig. 24(a)), only the strongest target is correctly detected while only few plots are generated for other possible targets. Even increasing the nominal P_{fa} value used for the CFAR threshold (see Fig. 25(a) for $P_{fa} = 10^{-3}$), the detection performance does not change while a larger number of false alarms arises (mainly detection of the sidelobes of the waveforms used).

The results show that with the ECA-B, many reasonably complete plot sequences are observed, while for the others only few plots are detected. It is also noted that the third acquisition of the sequence does not yield good detection performance with any of the algorithms due to the poor characteristics of this particular waveform. Even in this case, decreasing the detection threshold (see Fig. 25(b) for $P_{fa} = 10^{-3}$), the target detection capability is not significantly enhanced while many false alarms appear, which make the target plot sequences more difficult to recognize and hence reduces the capability to track potential targets. This is due the dynamic behaviour of the transmitted signals and shows how it can effect the resulting detection performance. This may be compensated to some extent by utilising other transmission channels.

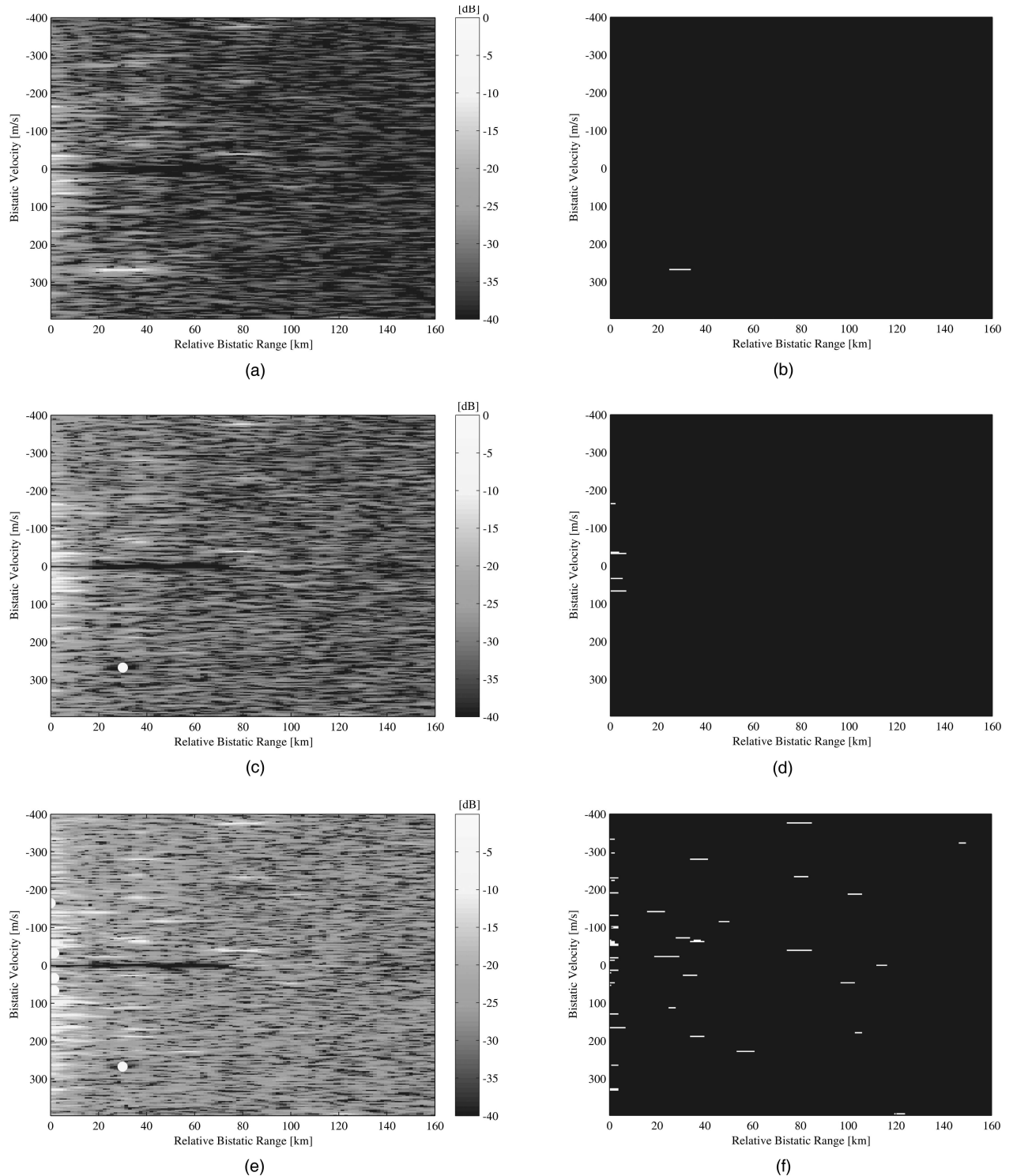


Fig. 22. Results for fourth file of real data set for ECA-B&S algorithm with parameters listed in Table II. (a)–(c)–(e) Shows 2D-CCF after stages 1–2–3. (b)–(d)–(f) Shows detection results after stages 1–2–3.

When using the ECA-B&S (see Fig. 24(c)), the completeness of the detected plot sequences is improved since additional plots are detected for a given target track. This gives a significant advantage especially for targets that result in only a 2-plot sequence when operating with the ECA-B, since their tracks are otherwise likely to be lost. Moreover, an

additional and quite complete sequence appears at about 60 km and -300 m/s which was not identified by the simpler algorithms. These advantages are obtained at the expense of a higher computational load. To counteract this problem a suboptimal implementation of the ECA-B&S algorithm was introduced in Section VC. This only performs a

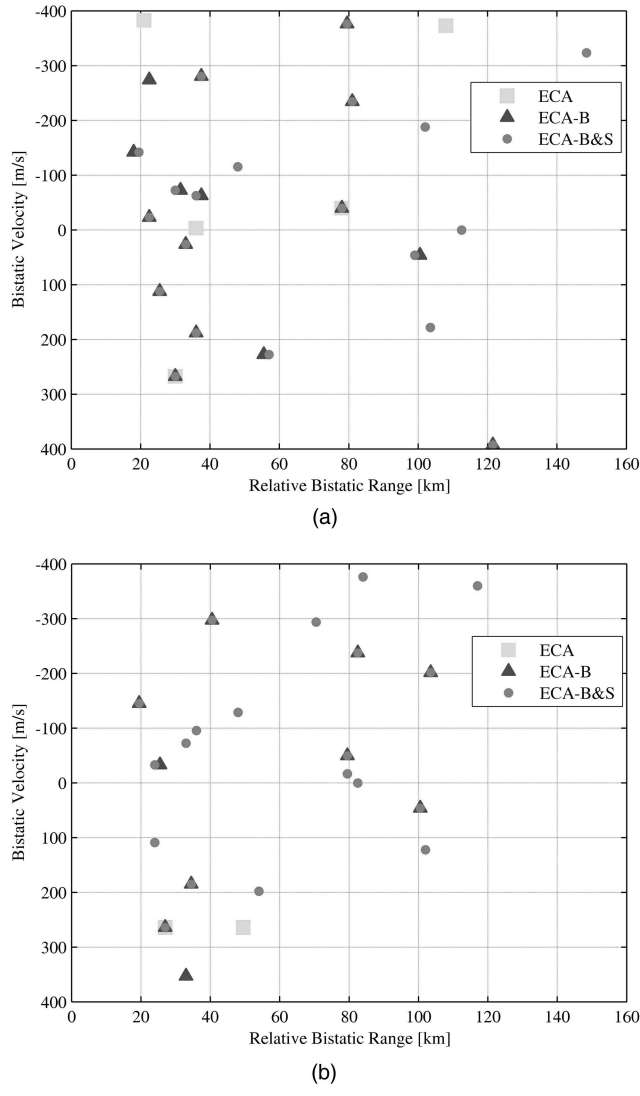


Fig. 23. Superposition of detection results obtained with ECA, ECA-B, and ECA-B&S. (a) Fourth file of real data set. (b) Fifth file of real data set.

cancellation over a limited mask at each stage. The results of the application of this suboptimal implementation of the ECA-B&S on the sequence of all 6 data files are shown in Fig. 24(d). As for the simulated case, even though the computational load has been dramatically decreased, this algorithm gives similar detection performance since the same target plot sequences can be detected with a comparable number of possible false alarms.

The results shown in this paper are but a few examples of an extensive analysis that has been performed on simulated and real data recorded on multiple acquisition campaigns. In all the cases considered similar considerations apply to the comparison among the different algorithms. The real data detection results have been compared against real data from a Mode S/ADS-B receiver (Kinetic Avionic) thus verifying their consistency with respect to the “ground-truth.” Moreover, it is possible to assert that qualitatively the rate of false alarms is largely

consistent with the rate obtained against simulated data.

VII. CONCLUSIONS

A multistage processing approach has been developed that enables effective disturbance cancellation as well as improved target detection for PBR systems. It is based on projections of received signals in a subspace orthogonal to both the disturbance and to previously detected targets. By operating on a set of small consecutive batches covering the whole integration time, a better disturbance cancellation and enhanced overall performance is achieved since a wider notch in the Doppler dimension of the filter is obtained. By applying consecutive stages of the algorithm it is possible to remove strong target echoes which otherwise mask weaker targets. The approach has been shown to be effective against typical simulated scenarios with a limited number of stages. The

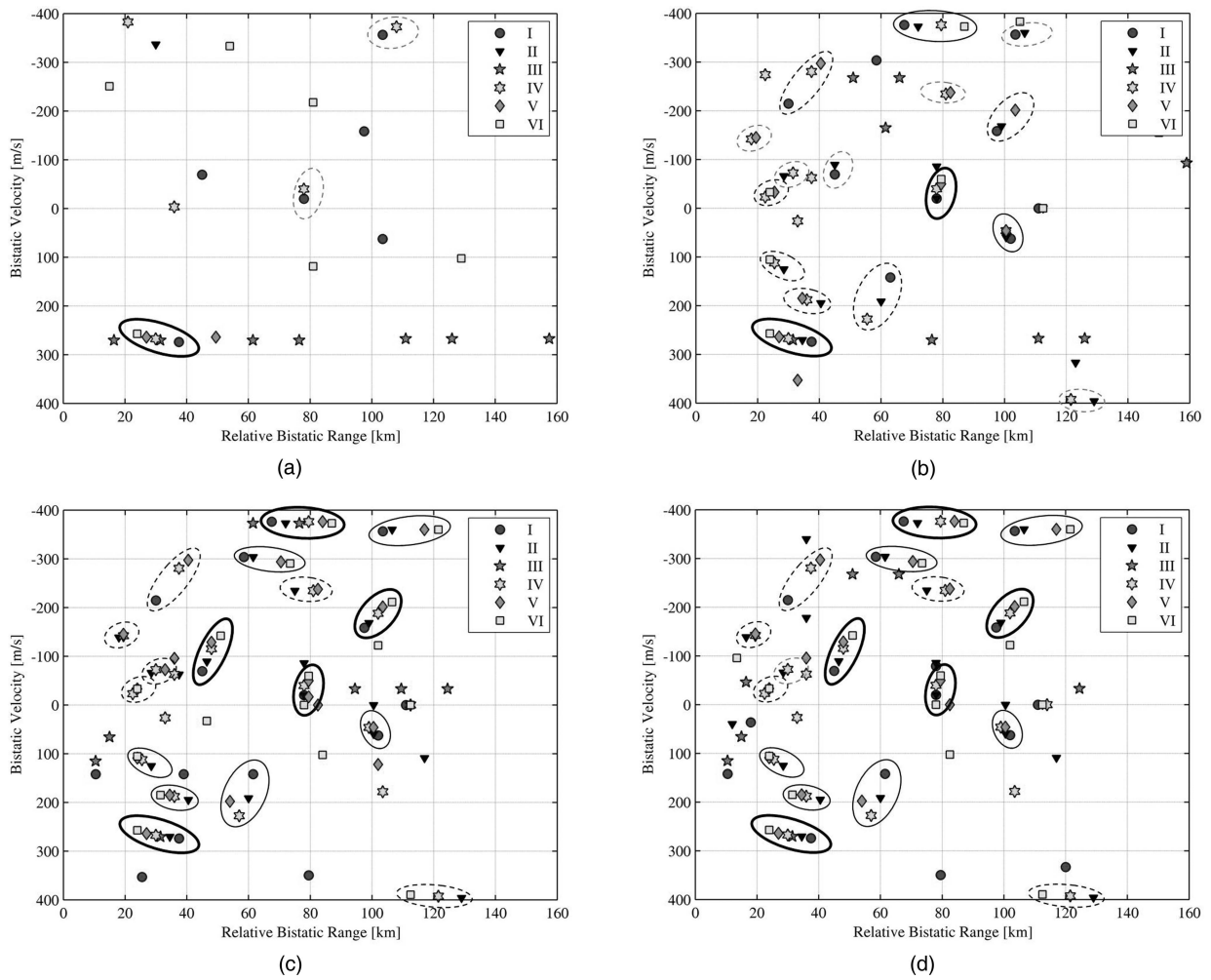


Fig. 24. Superposition of detection results over data files sequence obtained with: (a) ECA only, (b) ECA-B, (c) ECA-B&S, (d) ECA-B&S suboptimal implementation.

application of the algorithm to a real data set has further demonstrated its suitability since it allows: 1) an adaptive growth of the cancellation mask which can cater for strong disturbance residuals and target echoes, 2) avoidance of false alarms due to the high sidelobes of the transmitted waveform ambiguity function, and 3) detection of the weakest targets otherwise obscured. Finally, a suboptimal implementation of the multistage algorithm has been introduced, aimed at reducing its computational load. The performed analysis of simulated and real data demonstrates that the two versions of the algorithm are quite comparable in terms of achievable performance while the suboptimal version allows a dramatic decrease of the computational burden.

ACKNOWLEDGMENTS

F. Colone and P. Lombardo gratefully acknowledge the support of Finmeccanica, by means of SESM and SELEX-SI, for the development of this work. In particular, the theoretical development of the processing algorithms presented in this paper was totally sponsored by Finmeccanica.

F. Colone also acknowledges the hospitality at UCL, where she spent six months of work during which the experimental acquisition system of UCL was greatly improved to achieve very high quality data, the processing techniques were tested against the collected data and this manuscript was prepared.

REFERENCES

- [1] *IEE Proceedings on Radar, Sonar and Navigation* (Special Issue on Passive Radar Systems), **152**, 3 (June 2005), 106–223.
- [2] Griffiths, H. D., and Long, N. R. W. Television based bistatic radar. *IEE Proceedings, Pt. F (Communication Radar Signal Processing)*, **133**, 7 (1986), 649–657.
- [3] Howland, P. E. Target tracking using television-based bistatic radar. *IEE Proceedings on Radar, Sonar and Navigation*, **146**, 3 (1999), 166–174.
- [4] Howland, P. E., Maksimiuk, D., and Reitsma, G. FM radio based bistatic radar. *IEE Proceedings on Radar, Sonar and Navigation*, **152**, 3 (June 2005), 107–115.

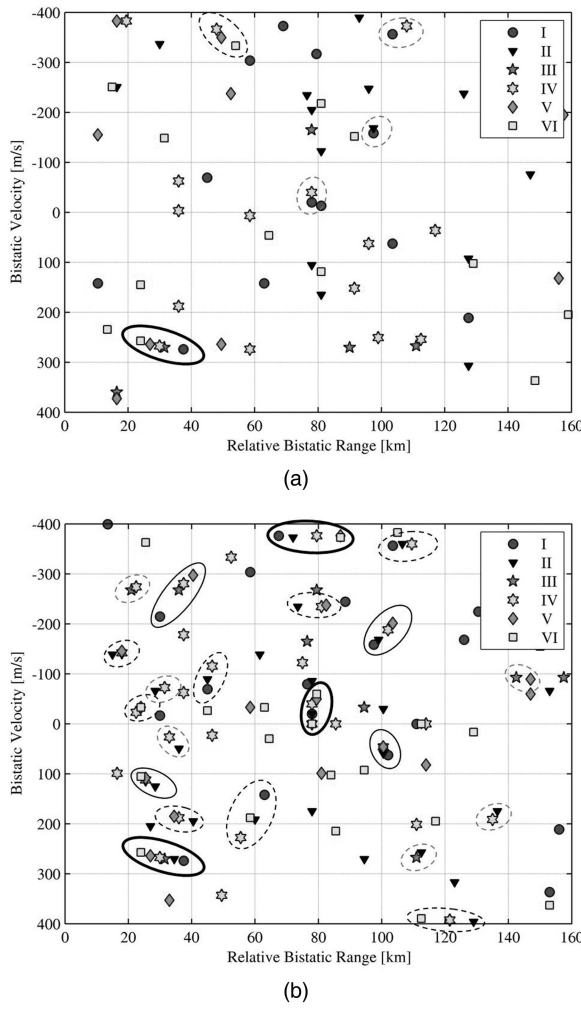


Fig. 25. Superposition of detection results over data files sequence obtained with: (a) ECA only, (b) ECA-B, with lower threshold ($P_{fa} = 10^{-3}$).

- [5] Griffiths, H. D., and Baker, C. J. Passive coherent location radar systems. Part 1: Performance prediction. *IEE Proceedings on Radar, Sonar and Navigation*, **152**, 3 (June 2005), 153–159.
- [6] Baker, C. J., Griffiths, H. D., and Papoutsis, I. Passive coherent location radar systems. Part 2: Waveform properties. *IEE Proceedings on Radar, Sonar and Navigation*, **152**, 3 (June 2005), 160–168.
- [7] Griffiths, H. D., Baker, C. J., Ghaleb, H., Ramakrishnan, R., and Willman, E. Measurement and analysis of ambiguity functions of off-air signals for passive coherent localisation. *Electronics Letters*, **39**, 13 (2003), 1005–1007.
- [8] Lauri, A., Colone, F., Cardinali, R., and Lombardo, P. Analysis and emulation of FM radio signals for passive radar. Presented at the 2007 IEEE Aerospace Conference, Big Sky, MT, Mar. 3–10, 2007.
- [9] Kulpa, K. S., and Czekala, Z. Ground clutter suppression in noise radar. Presented at the International Conference on Radar Systems (Radar 2004), Oct. 2004.
- [10] Axelsson, S. R. J. Improved clutter suppression in random noise radar. Presented at the URSI 2005 Commission F Symposium on Microwave Remote Sensing of the Earth, Oceans, Ice, and Atmosphere, Apr. 2005.
- [11] Gunner, A., Temple, M. A., and Claypoole, R. J., Jr. Direct-path filtering of DAB waveform from PCL receiver target channel. *Electronics Letters*, **39**, 1 (2003), 1005–1007.
- [12] Kulpa, K. S., and Czekala, Z. Masking effect and its removal in PCL radar. *IEE Proceedings on Radar, Sonar and Navigation*, **152**, 3 (June 2005), 174–178.
- [13] Cardinali, R., Colone, F., Ferretti, C., and Lombardo, P. Comparison of clutter and multipath cancellation techniques for passive radar. Presented at the IEEE 2007 Radar Conference, Boston, MA, Mar. 2007.
- [14] Colone, F., Cardinali, R., and Lombardo, P. Cancellation of clutter and multipath in passive radar using a sequential approach. In *IEEE 2006 Radar Conference*, Verona, NY, Apr. 24–27, 2006, 393–399.
- [15] Cardinali, R., Colone, F., Lombardo, P., Cognale, O., and Cosmi, A. Multipath cancellation on reference antenna for passive radar which exploits FM transmission. Presented at the IET International Radar Conference (Radar 2007), Edinburgh, UK, Oct. 15–18, 2007.
- [16] Haykin, S. *Adaptive Filter Theory* (4th ed.). Upper Saddle River, NJ: Prentice-Hall, 2002.

- [17] Bongioanni, C., Colone, F., Bernardini, S., Lelli, L., Stavolo, A., Lombardo, P.
 Passive radar prototypes for multifrequency target detection.
 Presented at the Signal Processing Symposium 2007,
 Jachranka Village, Poland, May 24–26, 2007.

Fabiola Colone (S'02—M'06) received the laurea degree in communication engineering and the Ph.D. degree in remote sensing from the University of Rome “La Sapienza,” Rome, Italy, in 2002 and 2006, respectively.

She joined the INFOCOM Department, University of Rome “La Sapienza,” Italy, as a research associate in January 2006. From December 2006 to June 2007, she was a visiting scientist at the Electronic and Electrical Engineering Department of the University College London, UK. Her current research interests include passive coherent location for surveillance purposes, multi-channel adaptive signal processing, space-time adaptive processing (STAP) with application to mono- and bi-static radar systems. She is involved in scientific research projects funded by the Italian Space Agency, the Italian Ministry of Research and the Italian Industry. Her research activity has been reported in a number of publications in international technical journals and conferences.

Dr. Colone was currently on the organizing committee, as the Student Forum Cochair of the IEEE 2008 Radar Conference, Rome, Italy. She was among those who were awarded the Best Student Papers at the IEEE 2006 Radar Conference, Verona, NY. She is frequently a reviewer for *IEEE Transactions on Aerospace and Electronic Systems* and other technical international journals.



Daniel O’Hagan obtained a first class (1.1) B.Eng. Honours degree in electronic and computer engineering in 2003. In 2004 he obtained his M.Sc. in electronics and communications in N. Ireland. His M.Sc. project involved the analysis and measurement of coupled currents in the field of body-worn devices such as coupling from mobile phone antennas.

In December 2004, he commenced his Ph.D. research into the characterisation of a passive bistatic radar using FM radio illuminators of opportunity under the supervision of Professors Chris Baker and Hugh Griffiths.

Currently he is employed as a research scientist at FGAN, Bonn, Germany.





Pierfrancesco Lombardo (S'93—M'95) received the laurea degree in electronic engineering and the Ph.D. degree from the University of Rome “La Sapienza,” Rome, Italy, in 1991 and 1995, respectively.

In 1991–1992 he served as officer engineer at the Official Test Center of the Italian Air Force of Pratica di Mare. In 1994 he was research associate at the University of Birmingham, UK, while working in the SAR processing team of the Defense Research Agency in Malvern, UK. During 1995 he was research associate at Syracuse University, New York. In June 1996 he joined as research scientist at the University of Rome “La Sapienza,” where he is presently full professor. His main research interests are in adaptive radar signal processing, radar clutter modelling, mono- and multi-channel coherent radar signal processing, SAR image processing and radio-location systems. In such areas, he has been project manager of a number of research projects funded by the Italian Space Agency, the Italian Ministry of Research, and the Italian radar industry. His research has been reported in over a hundred publications in international technical journals and conferences.

Dr. Lombardo was the Technical Cochairman of the 2008 IEEE Radar Conference, Rome, Italy. He served as Technical Chairman of the IEEE/ISPRS Joint Workshop on Remote Sensing and Data Fusion over Urban Areas (Rome 2001, Berlin 2003, Tempe 2005). He gave tutorial lectures and served in the technical committee of many international conferences on radar systems and signal processing. He is associate editor for radar systems for the *IEEE Transactions on Aerospace and Electronic Systems*. In 2001, he received the Barry Carlton Award for the best paper published in the *IEEE Transactions on Aerospace and Electronic Systems*. He received the prize of the best paper published in the *IEEE Transactions on Geoscience and Remote Sensing* in 2003.



Chris Baker is the Thales-Royal Academy of Engineering Professor of intelligent radar systems based in the Electronic and Electrical Engineering Department of University College London.

He has been actively engaged in radar system research since 1984 and is the author of over one hundred and fifty publications. His research interests include coherent radar techniques, radar signal processing, radar signal interpretation, electronically scanned radar systems, natural echo locating systems, and radar imaging.

Professor Baker is the recipient of the IEE Mountbatten premium (twice), the IEE Institute premium and is a Fellow of the IEE. He is also currently Chairman of the IEE Radar, Sonar and Navigation Systems Professional Network. He is a visiting professor at the University of Cape Town and also at Cranfield University. In September of 2008 he will take up the position of Dean of Engineering and Computer Science at the Australian National University.